ELSEVIER

Contents lists available at ScienceDirect

Journal of Materials Research and Technology

journal homepage: www.elsevier.com/locate/jmrt





In-situ and interrupted cyclic three-point bending tests in SEM of two pearlitic steel microstructures: Lamellar and partially spheroidized

Pablo Bruno Paiva Leão ^{a,b}, João Rodrigues de Barros Neto ^c, Samuel Filgueiras Rodrigues ^{a,d,*}, Maria Veronica Goncalves Rodrigues ^d, João Victor Barroso Xavier ^a, Tiago Nunes Lima ^b, Gedeon Silva Reis ^d, Antonio J. Ramirez ^e, Hamilton Ferreira G. de Abreu ^a

- ^a Materials Characterization Laboratory (LACAM), Department of Metallurgical and Materials Engineering, Federal University of Ceará, Campus Do Pici, Bloco 729, Fortaleza, 60020-181, CE, Brazil
- b SENAI CIMATEC, SENAI Innovation Institute for Conformation and Joining Materials (ISI-C&UM), Orlando Gomes, 1845, 41650-010, BA, Brazil
- c Department of Materials Engineering, Federal University of Piaui, Technology Center, Federal University of Piauí (UFPI), Teresina, 64049-550, PI, Brazil
- d Graduate Program in Materials Engineering, Federal Institute of Education, Science and Technology of Maranhao, Sao Luis, 65030-005, MA, Brazil
- e Department of Materials Science and Engineering, The Ohio State University, Fontana Laboratories Suite 2136 140 W. 19th Avenue, Columbus, OH, USA

ARTICLEINFO

Keywords: Pearlitic steel Stress-relief treatment In-situ microstructure characterization Cyclic three-point bending test Deformation and fracture behavior Interrupted EBSD Transmission-EBSD

ABSTRACT

Lamellar and partially spheroidized pearlitic microstructures were lab-manufactured via, respectively, stress relief treatment at 400 (SR400) and 700 °C (SR700) for 60 s. The performance of both microstructures under four successive three-point bending (TPB) tests was investigated via in-situ secondary electron imaging in scanning electron microscopy. Additionally, consecutive interruptions after each TPB were performed for electron back-scatter diffraction (EBSD) analyses. Transmission-EBSD and scanning transmission electron microscopy were employed in the starting specimens: SR400 and SR700. Initially, SR400 presented many shear bands, while SR700 depicted small recrystallized grain zones with coarse spheroidized cementite. Additionally, Bagaryatskii and Isaichev cementite/ferrite orientation relationships were found for SR400 and SR700, respectively. During TPB deformation, SR400 exhibited high strength and stable mechanical behavior, while SR700 displayed a softening phenomenon and earlier failure. Moreover, the EBSD analyses indicated that strains were concentrated in the shear bands of SR400 and the small recrystallized grain zones of SR700 during TPB. The small recrystallized grain zones with coarse spheroidized cementite were related to promoting the earlier damage and, consequently, failure of SR700. Finally, the more significant presence of sheared areas and elongated dimples on the SR400's fractured surface demonstrated its higher capacity to support plastic deformation under TPB than SR700.

1. Introduction

Tensile armor layers on unbonded flexible pipelines (risers) are typically made of several rectangular pearlitic steel wires, which are, together, helically twisted around the pipeline structure. The crucial role of the tensile armor is to ensure a good balance of axial rigidity and flexibility in risers. In addition to this, these pearlitic steel layers must support all the riser weight and transfer the load to the vessel infrastructure on the sea surface. In view of this, these flat wires are, in general, produced throughout a particular manufacture route for obtaining the mechanical properties required by the tensile armor

application: hot-rolling \rightarrow patenting treatment \rightarrow cold forming (drawing, rolling, or drawing + rolling) \rightarrow stress relief treatment \rightarrow re-winding wire into bobbins \rightarrow helical twisting process [1–3].

Concerning specifically the process of re-winding wire into the bobbins (RWWB), this procedure starts with the pearlitic steel wire in a stress-relieved condition wound in coils. In this case, the wire has an arch shape along its length due to the coil curvature. This circumstance induces an initial bending state in the component. Next, the wire is initially unwound from the coil and follows an arduous deformation path through two distinct roller machines (pinch and casting rollers) arranged in sequence. Based on this, the pearlitic wire is first stretched in

E-mail address: samuel.filgueiras@ifma.edu.br (S.F. Rodrigues).

^{*} Corresponding author. Materials Characterization Laboratory (LACAM), Department of Metallurgical and Materials Engineering, Federal University of Ceará, Campus do Pici, Bloco 729, Fortaleza, 60020-181, CE, Brazil.

the pinch rollers to eliminate the starting arch profile. Then, the straight flat wire goes to the casting rollers comprising two succeeding rolls. In this setting, the wire passes below the first roll and goes up above the second roll. In this case, the wire follows, consecutively, the opposite concavities shape of the two rolls. As a result, the wire undergoes two more similar bending deformations during its passage through the casting rollers apparatus. The RWWB operation ends up with the rewinding wire into bobbins, which establishes one more bending condition. This deformation practice guarantees the integrity of the wire in the bobbin and its defect tolerance. Therefore, after stress relief, the wire is submitted to a repeated bending condition during the RWWB process, establishing a new residual stress state in the pearlitic microstructure [3]. Based on this, the initial stress-relieved pearlitic steel wire should be mechanically suitable for overcoming that rigorous deformation process without failure.

In this regard, pearlitic steels present a great combination of high strength and good ductility, which makes them broadly employed in wire-related applications as tensile armor layers. This mechanical balance is manageable by controlling the set of variables related to the pearlitic microstructure, including its morphology. In most cases, the refined lamellar morphology (alternated nanometric layers of soft ferrite and hard cementite) is adopted in practices that require high strength (ultimate tensile strength or yield strength) with a satisfactory ductility performance [4]. This fact is attributed to the Hall-Petch relationship that is followed by the pearlitic interlamellar spacing [5]. In this way, fine lamellar morphology is usually obtained through the patent treatment that enables a fast and isothermal eutectic transformation from austenitic temperatures [6]. Likewise, regarding flat pearlitic steel products, the lamellar morphology is still preserved after cold-rolling and some fast thermal treatments (annealing and stress relief treatments) [7.8].

Otherwise, an increase in ductility accompanied by a reduction in strength can be designed through the partial or total spheroidization of the cementite from its starting lamellar structure. In the past, this morphological modification was obtained via many hours of heat treatment at temperatures below A1. However, nowadays, there are many faster ways to produce spheroidized cementite particles. For instance, Stodolny et al. [9] accomplished the spheroidization process at 700 °C for an hour by reducing the initial interlamellar spacing. In this regard, aluminum (strong ferrite stabilizer) content in high-carbon steels can lead to a faster process of cementite spheroidization by refining the prior pearlitic interlamellar spacing during the eutectoid transformation [10]. Moreover, it is possible to produce spheroidal cementite by the divorced eutectoid transformation (DET) [11]. The DET thermal treatment consists of two subsequent steps: an austenitization and an isothermal transformation, both in temperatures close to A₁. In this context, the presence of chromium optimizes the process of cementite spheroidization during the DET [12]. Moreover, the introduction of a prior warm rolling deformation minimizes the hold time of the succeeding spheroidization treatment [12,13]. Additionally, some researchers [8,14] observed that introducing a prior cold-rolling deformation in pearlitic steels resulted in partial or total spheroidization of cementite after a few seconds at 700 °C.

Concerning pearlite deformation, the ferritic matrix has lower yield strength than the cementite phase [15]. In that manner, the ferrite is prone to achieve an earlier plastic state than cementite during the progress of deformation [16]. In this scenario, dislocations can be nucleated at the cementite(θ)/ferrite(α) interface and glide throughout the ferritic matrix. However, further dislocation slippage can be hindered for other cementite structures spread in the matrix. In this way, piles-up of dislocation can occur. This restriction in dislocation movement increases the required stress to keep the material deforming (strain-hardening) [17]. Therefore, the cementite morphology plays a crucial role in strain-hardening behavior in pearlitic steels. Taking this

into account, it is pointed out from the literature [18–20] that the strain-hardening rate depends on the loading direction, the thickness and crystallographic orientation of the ferrite layers in pearlitic steels with lamellar microstructure. It implies that in the lamellar microstructure, the high strain-hardening rates are achieved when the activated systems in ferrite have small Schmid factors and short mean-free paths.

Otherwise, in the spheroidized condition, the strain-hardening rate is proportional to the square root of the division between the volume fraction and the average size of the cementite particles [18]. Moreover, Zheng et al. [21] have observed that the strain-hardening increases from a fully spheroidized to a completely lamellar pearlitic microstructure due to the effective barrier provided by the lamellar shape against the dislocation movement. Furthermore, these authors noticed the highest strain-hardening for a pearlitic microstructure with a mix of lamellar and spheroidized cementite. They explained that this morphological merger raises the amount of θ/α interfaces, enhancing dislocation nucleation during plastic deformation. In addition to this, the study of Zhou et al. [22] describes that amorphous cementite can absorb dislocations while crystalline ones do not. However, Tagashira et al. [23] proposed that crystalline cementite can activate multiple slip systems during plastic deformation to maintain the compatibility between ferrite and cementite phases. They also reported that this mechanism of cementite deformation depends on other features, such as the θ/α orientation relationship (OR). Moreover, the initial dislocation density also affects the strain-hardening rate of carbon steels [18,24].

Additionally, the behavior of the pearlitic wires under the RWWB deformation can be la-simulated by implementing several bending cycle proceedings [25]. Within this scope, bending experiments develop a stress gradient throughout the specimen's thickness [26]. In particular, the longitudinal thickness fibers near the top surface (in touch with the punch) and the bottom surface (in contact with the support pins) undergo compression and tensile stresses, respectively. Conversely, the middle thickness region remains in a neutral stress state. Also, recent works [8,26-28] reported that the outer tensile fiber is prone to produce local deformations (shear bands) that lead to the beginning of catastrophic failure during the bending experiments. In particular, Kapp et al. [26] demonstrated that the lamellar architecture of the pearlitic morphology retards the development of shear bands and their propagation, which delays the damage initiation. However, the introduction of cyclic bending arrangements imposes recurrent compression-tensile stresses in both aforementioned outer fibers of the specimen. In this regard, pearlitic steels can experience hardening and softening (Bauschinger effect) mechanisms. The Bauschinger effect is usually related to the rearrangement and annihilation of dislocations due to their reservable motion [29]. Finally, Leão et al. [8] lab-produced flat pearlitic steel under different process routes based on the actual manufacture of tensile armor wires. The authors noticed a harmful pearlitic microstructure that quickly failed under cyclic bending deformation. This microstructure with small ferritic recrystallized grains and partial spheroidized cementite was obtained by applying a stress relief treatment at 700 °C for 60 s in a deformed lamellar pearlitic microstructure with a {111} <112> predominantly ferritic crystallographic orientation. On the other hand, the lamellar structure was maintained under stress relief at 400 $^{\circ}\text{C}$ for 60 s. Therefore, to deeply investigate this issue, the present work focused on evaluating the performance of these microstructural pearlitic conditions under cyclic three-point bending (TPB) circumstances. In-situ secondary electron imaging was employed during the TPB operation inside a scanning electron microscopy. In addition to this, high-resolution techniques (transmission electron backscattered diffraction and scanning transmission electron microscopy) and EBSD interrupt analyses were employed in this investigation to supply rich details about the starting specimens and their behavior under cyclic bending deformations.

2. Materials and methods

2.1. Specimens processing

In this work, a lab-simulated process route, illustrated in Fig. 1, was performed in a commercial SAE 1075 pearlitic steel. This lab operation was planned based on actual manufacturing processes of rectangular wires employed on flexible pipelines as tensile armor [1-3]. The chemical composition of the as-received pearlitic steel is provided in Table 1. Within the lab-simulated route scope, the rolling processes (hot and cold) were carried out by using a rolling machine with a roll diameter of 110 mm and a rolling speed of 8 m/min. The temperatures of the specimen and the bath salt (60 % potassium nitrate + 40 % sodium nitrate), respectively, in the hot rolling process (HRP) and the patent treatment (PT) were measured via an infrared thermometer. A muffle furnace was employed in the HRP, PT, and stress relief (SR) treatments. Concerning the HRP, a start rectangular specimen (thickness $\approx 8 \ mm \ x$ length \approx 40 mm x width \approx 50 mm) underwent an initial rolling pass of adjustment (≈0.3 mm thickness of reduction) immediately after its austenitization at 1050 °C for 600 s. Subsequently, the specimen was quickly put back in the furnace at 1050 °C and kept in there for 60 more seconds, followed by an additional regular hot pass (≈0.6 mm of reduction). The last procedure was repeated six times, succeeded by a final air cooling. The final sample's thickness was \approx 4.4 mm (\approx 45 % of hot reduction), and the average finish rolling temperature was 906 °C. After the HRP, the PT treatment was applied in the 45 % hot reduced specimen. This PT consisted of an initial sample's austenitization (at 950 °C for 390 s) and its direct quenching in a bath salt (at 550 °C for 40 s) followed by a final air cooling step. Then, the patented specimen was 65 % cold rolled (at a rate of ≈0.1 mm/pass), achieving a final thickness of \approx 1.54 mm. After that, the 65 % cold rolled specimen was cut into a smaller rectangular dimension of $\approx\!26$ (length//rolling direction) $x\sim10$ (width) $x \sim 1.54$ (thickness) mm³. Then, the resized samples in the cold

rolled condition received two different SR treatments at 400 and 700 $^{\circ}$ C using the same holding time of 60 s. As a result, the two final lab-processed conditions of SAE 1075 pearlitic steel used in this study were named SR400 and SR700, as shown in Fig. 1. In addition to this, in the actual production route, the following process step that succeeds the SR treatment is the re-winding wire process [3]. The re-winding wire operation is usually lab-simulated via alternated successive bending tests [25] that are the focus of a further section.

2.2. Tensile test, scanning transmission electron microscopy (STEM) image, and transmission electron backscatter diffraction (t-EBSD) analysis

Tensile tests were performed for the two stress-relieved pearlitic steel states (SR400 and SR700) by using a universal testing machine (landmark 370.10 with a maximum load of 100 kN). The tensile samples were machined according to the ASTM E8/E8M standard concerning the tensile direction parallel to the rolling direction. Then, the elastic modulus, yield strength, ultimate tensile strength, resilience, toughness, and maximum elongation were obtained from the tensile test curves (Engineering stress vs Engineering strain) of SR400 and SR700 pearlitic steel conditions. In this case, the maximum elongation and ultimate tensile strength were determined, respectively, by the final elongation at the failure point and the maximum stress value sustained for each sample during the tensile test. Moreover, the elastic modulus was calculated based on the slope of the straight line in the elastic portion of the tensile test curves. Regarding the yield strength, it was defined by the point where a line, introduced parallel to the linear portion of the tensile test curves and starting at 0.2 % strain, intercepts the Engineering stress vs Engineering strain curves. Finally, the resilience and toughness were acquired by the measurement of the respective following areas below the Engineering stress vs Engineering strain curves: elastic portion area (delimitated by the yield strength) and the total area (up to the specimen failure).

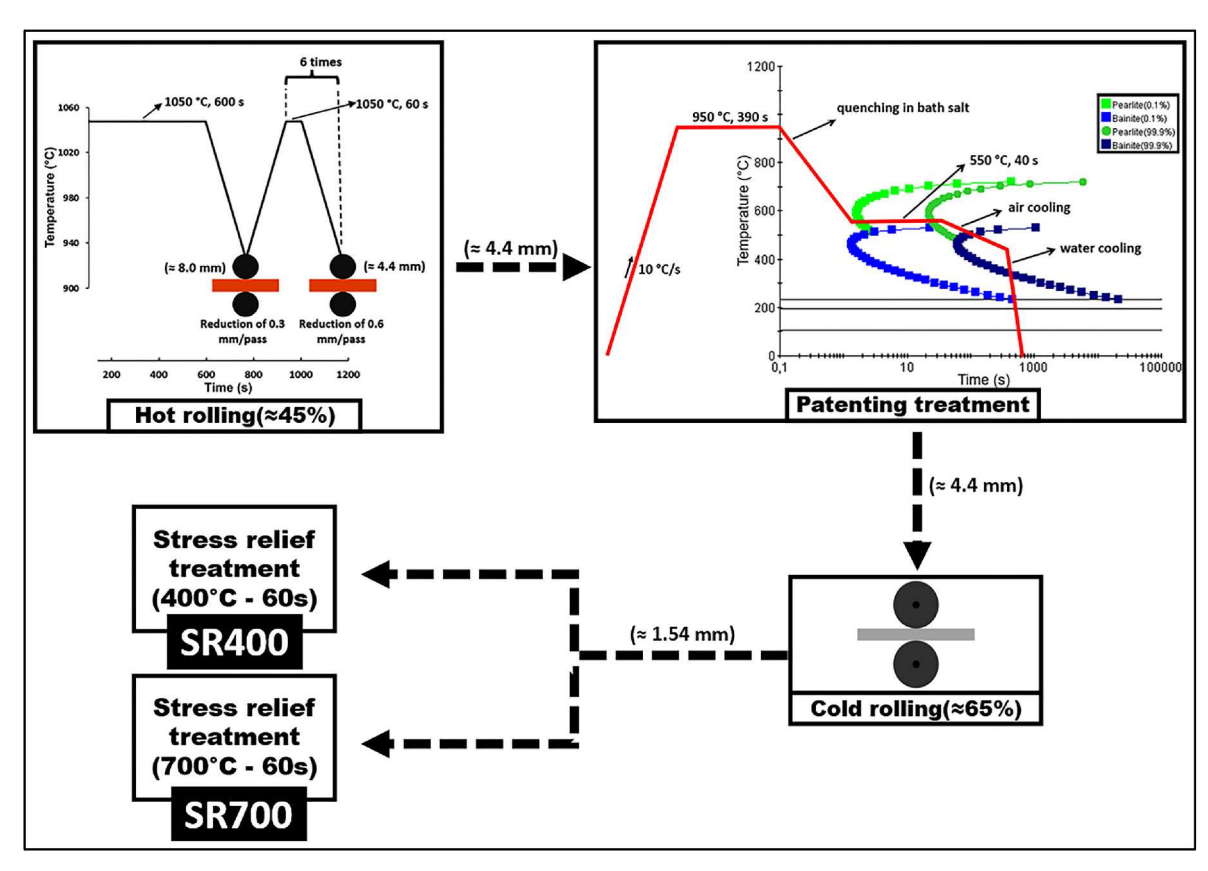


Fig. 1. Flowchart sketch of the lab-simulated processing route performed in the present study. The numbers in millimeters (mm) represent the sample's thickness.

Table 1
Chemical composition of the as-received pearlitic steel (wt%).

С	Mn	Si	S	P	Cr	Ni	V	Al	Ti	Fe
0.736	0.648	0.227	0.006	0.011	0.179	0.023	0.004	0.023	0.003	Bal.

Additionally, a THERMO SCIENTIFIC APREO field emission gun (FEG) scanning electron microscope (SEM) coupled with an EDAX EBSD detector was adopted to carry out the scanning transmission electron microscopy (STEM) image and transmission electron backscatter diffraction (t-EBSD) techniques in the SR400 and SR700 specimens. In this case, a thin rectangular foil was obtained from each investigated sample. The transparent foils were shaped and prepared through a focused ion beam (FIB) microscope (Helios NanoLab 600 DualBeam Field Emission Gun). Also, in the FIB procedure, a small amount of amorphous platinum was inserted in the tip of the foil's edge to correct the background of the Kikuchi diffraction patterns during the t-EBSD performance. Regarding the stress-relieved specimens, the transparent foils were obtained in a position parallel to the longitudinal section from the normal surface area. It means that the analyzed areas were delimitated by the normal direction (ND) and rolling direction (RD). Then, the transparent specimens were mounted in a proper holder. For the acquisition of high-resolution images, the STEM detector was placed below the thin foil that was perpendicular to the incident electron beam. This operation was performed by employing an accelerating voltage of 30 kV, a current of 50 pA, and a working distance (WD) of 10 mm. While for the t-EBSD analyses were implemented, an operating voltage of 20 kV, a step size of 1.6 nm, a WD of 5 mm, and a sample tilt angle of -20° . Finally, (100), (110) and (111) pole figures were plotted for ferrite and cementite from five t-EBSD maps.

2.3. In-situ and interrupted three-point bending experiment

To simulate the behavior of pearlitic steel under the re-winding wire operation [3], the two lab-manufactured pearlitic conditions (SR400 and SR700) were submitted to a three-point bending (TPB) test. This experiment was conducted by using a kammrath-weiss tensile-compression stage (maximum loading of 5 kN) integrated with a special adapter MZ. V32 for the TPB procedure (see Fig. 2(a)). In this context, the TPB experiment was run at room temperature with a maximum loading pin (central pin or punch) displacement of 2.5 mm, a length between the support pins (outer pins) of 26 mm, and a constant displacement rate of 5 μ m/s. The longitudinal section (rolling direction x normal direction) of the rectangular samples was the inspected region. In addition, the bending investigation was comprised of four consecutive bending cycles by alternating the superior and inferior sample surfaces in contact with the pins. This is illustrated in the schemes shown in Fig. 2 (b) and (c). In this way, the bending conditions were labeled according to the resultant amount of consecutive bending undergone in the sample. For instance, "B1", "B2", and "B3" represent the bent samples in the maximum displacement (2.5 mm) of the loading pin, respectively, after the first, second, and third subsequent alternated bending procedures. However, "B4" was bending up to the point where the specimen failed during the fourth consecutive bending step. In this case, the displacement of "B4" will depend on the material's bending resistance. Moreover, "B0" symbolizes the unbent condition, which means the initial stress-relieved specimen state. Also, the displacement direction of "B1" was referenced as a positive bending direction. In this way, "B2" and "B4" displace in a negative direction about "B1" and "B3". Moreover, the conditions named "After B1", "After B2", and "After B3" mean, respectively, that after the first, second, and third consecutive bending, the specimens were bent back up to the initial displacement position of the loading pin, which refers to the location of 0 mm in displacement. Likewise, the "During B4" condition was performed after four consecutive bending procedures. However, "During B4" was not brought back to the initial position; instead, the central pin moved until 1.17 mm

during the fourth bending step, which was determined by the earlier failure of the SR700 pearlitic conditions.

Furthermore, the acquisition of the in-situ secondary electron (SE) images was carried out by setting the Kammrath-weiss stage inside the chamber of a THERMO SCIENTIFIC QUATTRO FEG SEM. These SE images were captured in a resolution of 1536 \times 1024 pixels. The SEM operation was conducted by using an accelerating voltage of 5 kV, a current of 0.18 nA, and a working distance (WD) of 13.5 mm. More specifically, SE images in low magnification (macro) were obtained in real time throughout the experiment's progress. Otherwise, SE images in high magnification (micro) were taken on two pre-selected regions that were located around 100 nm below the external surfaces (top and bottom) and aligned to the loading pin. In this regard, the two initially chosen regions were tracked and micro-photographed only at the maximum displacement periods (B0, B1, B2, and B3). Fig. 2(b) shows a schematic sketch of these displacement instants where the red squares represent the captured micro image zones. Additionally, the fourth consecutive TPB step of the investigated conditions (SR400 and SR700) was set to run up to their failure, aiming to evaluate the samples' resistance under the final accumulated bending state. Additionally, the fractography was obtained by using an accelerating voltage of 20 kV, a current of 3.2 nA, and a WD of 8.5 mm in the THERMO SCIENTIFIC QUATTRO SEM. Finally, the digital image correlation (DIC) technique was applied to the recorded micro SE images. In this regard, the opensource 2D-DIC MATLAB software (Ncorr v1.2) was adopted to compute the Eulerian strain (e_{vv}). A subset size of 55 pixels and a subset space of 1 pixel were chosen for the DIC proceeding.

Moreover, to assess the lattice strain behavior after each bending procedure of the SR400 and SR700 specimens, an electron backscatter diffraction (EBSD) examination was adopted on an area located around 100 nm from the top surface and aligned to the loading pin. This EBSD investigation region was chosen because the failure started on the top side under tensile stress during the fourth bending test. In this context, the same corresponding EBSD region was evaluated in the unbent condition (B0) and after introducing successive bending steps (After B1, After B2, and After B3). On this point, the fourth bending procedure in both specimen conditions was performed up to the earlier failure of SR700 (at 1.17 mm elongation) to compare them (SR400 and SR700) under the same final bending circumstance. In this setting, Fig. 2(c) depicts an illustrative diagram of the sequence of the EBSD analyses where the red squares are the EBSD evaluated zone position. Additionally, in this case, the interrupted TPB tests were implemented outside the SEM chamber with interruptions for the EBSD investigations. A THERMO SCIENTIFIC APREO FEG-SEM coupled with an EDAX EBSD detector was adopted to perform the EBSD procedures with an operating voltage of 20 kV, a step size of 50 nm, a WD of 8 mm, a sample tilt angle of 70° and a square grid system.

The rectangular samples were mounted in resin for metallographic preparation. For in-situ SE imaging, the longitudinal section of the specimens was grounded (using sandpapers from #240 to #2000 grit), polished (using diamond suspensions of 6, 3, and 1 μm), and etched with 4 % nital solution. An indentation reference was inserted in the middle thickness of the samples to ensure that the loading pin was placed in the correct position during the bending cycle transition. Regarding the EBSD analyses, the longitudinal section of the specimens mounted in resin also received the regular metallographic preparation just described above (grounding and polishing) with an additional vibratory polishing (with 0.04 μm colloidal silica), and no etch was applied to them. After the samples' preparation, the mounting resin was removed via its dissolution in acetone. Finally, the EBSD data were evaluated through TSL OIM

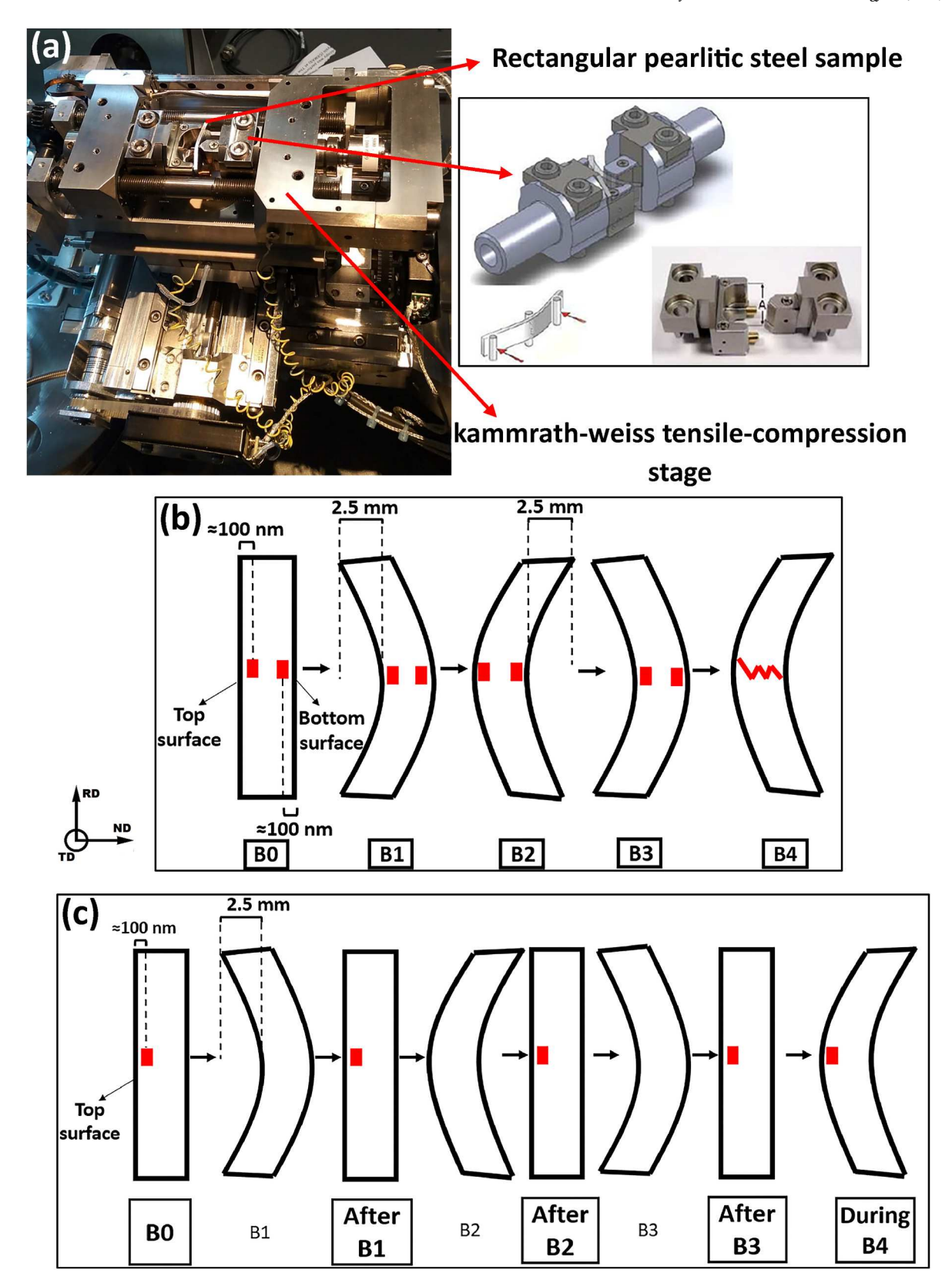


Fig. 2. Details of the in-situ and interrupted three-point bending (TPB) experiments carried out in this work. (a) Kammrath-Weiss tensile-compression stage coupled with an adapter MZ. V32 for the TPB tests. (b) Schematic sketch of the areas (red squares) where the high magnification secondary images were acquired during the in situ TBP performance. (c) Illustrative scheme of the region (red squares) where the electron backscattered diffraction analyses were performed during the interrupted TPB operation.

software, and their inverse figure pole (IPF) maps were plotted in the z-direction.

3. Results and discussion

3.1. The characteristics of the starting pearlitic steel before the in-situ bending experiment

This section aims to describe the main microstructural and mechanical differences between the initial unbent steel states (SR400 and SR700) studied in this work. In addition to this, the present topic provides some possible θ/α ORs for both starting conditions. In this way, Fig. 3 exhibits the SE micrograph, the STEM bright field image, and the map of grain boundary distribution for the SR400 and SR700 specimens. In detail, Fig. 3(a) and (c) show that the SR400's microstructure mainly consists of lamellar pearlitic morphology with its interlamellar spacing

around 173.2 (±37.6) nm. Moreover, it is possible to observe in Fig. 3(a) some narrow tilted regions with bent cementite lamellae (identified by yellow arrows). This locally damaged cementite suggests the presence of shear bands [8]. Also, it is pointed out (by yellow arrows) in Fig. 3(c) many dark contrast lines connecting two following lamellar cementite. This sort of demarcation is often acknowledged as cell or subgrain boundaries [30–32]. These substructures found in SR400 were likely generated during the prior 65 % cold rolling process. Therefore, the resultant SR400 microstructure indicates that the combined low temperature with the short holding time introduced during the stress relief treatment was insufficient to promote significant microstructural changes from the cold deformed state [8].

Otherwise, it can be seen in Fig. 3(b) and (d) that the SR700's cementite is comprised of a partially spheroidized structure with wormlike and spheroidal shapes. This fast process of cementite spheroidization, which means in just 60 s, may be attributed to the employment of

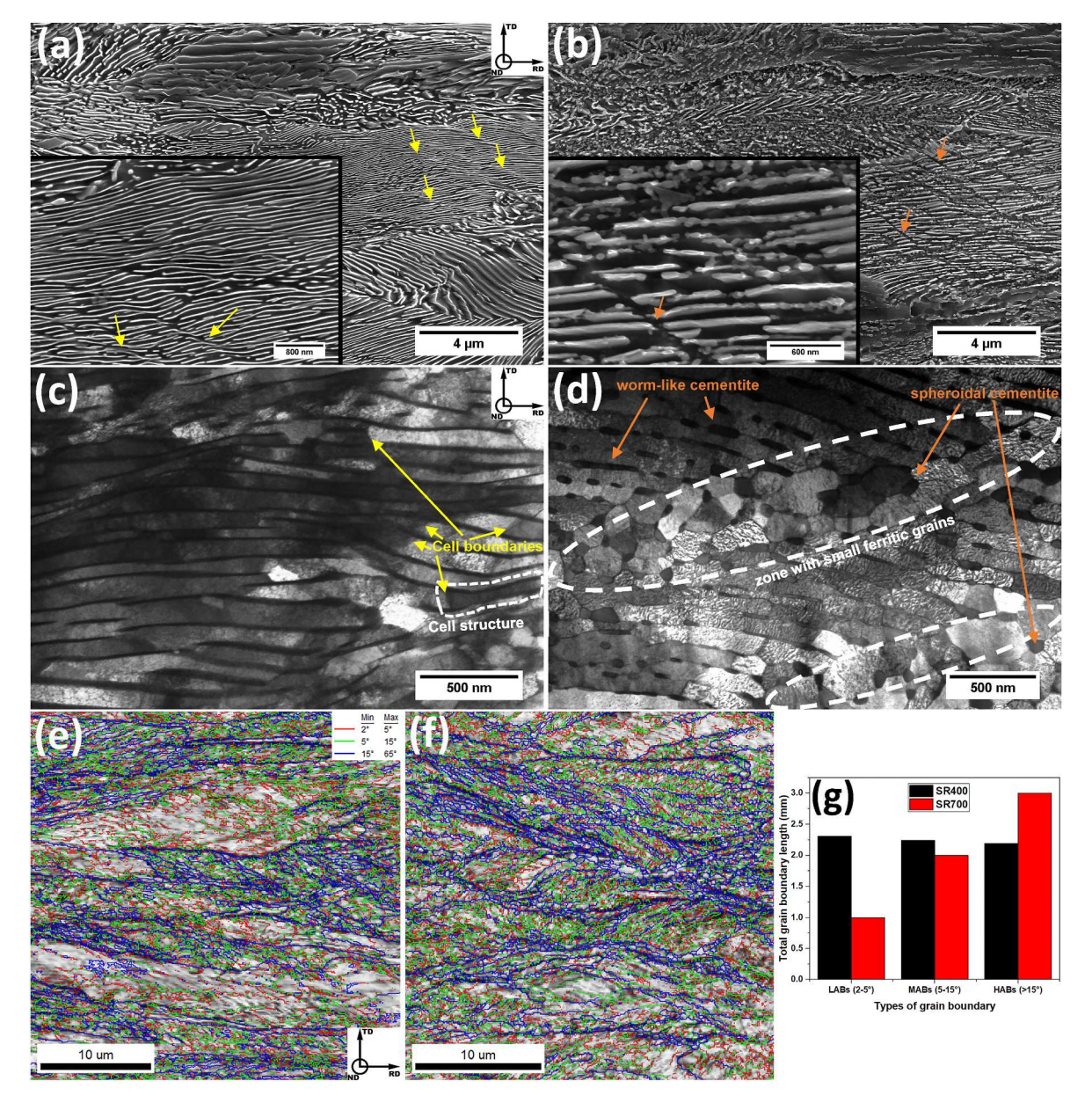


Fig. 3. Initial microstructural characteristics of the SR400 and SR700 conditions. Start secondary electron (SE) micrographs obtained via scanning electron microscopy, bright field images acquired via scanning transmission electron microscopy technique, and grain boundary distribution (GBD) maps collected via electron backscattered diffraction analysis, respectively, of (a) (c) (e) SR400 and (b) (d) (f) SR700 specimens. (g) The total length of the grain boundary types measured from the GBD maps of SR400 and SR700 conditions. The yellow and orange arrows in the SE micrographs indicate shear bands and disrupted cementite zones, respectively.

the high temperature (700 °C) in a high defect content microstructure introduced by the prior cold rolling stage [33,34]. Moreover, the orange arrows in Fig. 3(b) indicate narrow tilted zones where the cementite is disrupted. In addition, the white dashed circle in Fig. 3(d) delimitates an area that contains many small ferritic grains, which are surrounded by coarse spheroidal cementite particles at their grain boundaries and triple junctions. These grains follow an alignment pattern identical to the shear bands. In this context, Furuhara et al. [14] found small recrystallized ferritic grains in a 70 % cold rolled pearlitic steel after a short time thermal treatment at 700 $^{\circ}\text{C}$. They observed that the new small grains nucleated in the shear bands produced in the prior cold-rolling process. Also, the authors mentioned that the spheroidization of cementite starts earlier in high misorientation regions, such as shear bands of the ferritic matrix, where the cementite is heavily deformed. Likewise, Leão et al. [8] studied the same processing route of SR700 performed in this work. The authors revealed that small and recrystallized grains were nucleated in shear bands of {111}<112> orientated pearlitic blocks. However, they have detected these recrystallized ferritic grains via the EBSD technique. Therefore, it is reasonable to consider that the high-resolution STEM image can confirm the presence of the small ferritic grains in the SR700 condition.

Another point is that the SR700's ferritic matrix (in Fig. 3(d)) seems to have a stripped contrast. This phenomenon may be related to the carbon diffusion from cementite to the ferritic matrix, resulting in the Cottrell atmosphere [35]. This event becomes possible due to the higher binding energy between the carbon (C) atom and ferrite's dislocation compared to the C in cementite [36,37]. Therefore, the higher temperature (700 °C) during the stress relief treatment introduced in the 65 % cold rolled pearlitic condition may have led to the segregation of some C atoms to the dislocations' cores due to the establishment of a new and more stable energetic state [38]. However, this arrangement results in dislocations pinning. Consequently, these held dislocations are barely recovered during the thermal treatment and stay in the ferritic matrix, which explains the regions in the black contrast in Fig. 3(d). Additionally, Fig. 3(e) and (f) show the maps of grain boundary distribution for SR400 and SR700, while Fig. 3(g) displays the total length of the grain boundary type content on these maps. In this context, low-angle boundaries (LABs) and medium-angle boundaries (MABs) with ranges of local lattice misorientation, respectively, of 2-5° and 5–15°, are related to the presence of geometrically necessary dislocations (GNDs) [39]. Based on this, it is possible to realize that the high-stress relief temperature (700°) introduced in the SR700 condition resulted in a moderate total length decrease of LABs and MABs. However, there is still a considerable density of LABs and MABs spread throughout the SR700's ferritic matrix, as shown in Fig. 3(f). Therefore, these retained LABs and MABs may support the pinning effect of carbon on dislocations during the recovery process during the high temperature (700°C) thermal treatment.

Regarding the mechanical properties, Fig. 4 depicts the tensile test curves (engineering stress against engineering strain) for the SR400 and SR700 samples. This result indicates that SR400 has superior yield strength, ultimate tensile strength, and resilience, whereas SR700 presents higher values of maximum elongation and toughness. In this way, it is well known from the literature [40-42] that plastic deformation in ferritic matrix with body-centered cubic crystalline structure occurs based on dislocation's glides, and in pearlitic steels, the cementite lamellae act as barriers against the dislocation motion. Furthermore, the initial work-hardening state (dislocation density) can affect the required critical stress for starting the dislocation flow due to their own restrictive interactions (tangles and pile-ups) [17]. In this regard, the combination of the cementite in a lamellar geometry together with a significant degree of defects in the ferritic matrix can significantly make the movement of dislocations difficult. This may explain the higher resistance of SR400 to its permanent deformation and fracture. Conversely, the set of a partially spheroidized cementite shape and a slightly lower length of LABs and MABs retained in the ferritic matrix suggests a more effortless plastic flow. This justifies the more significant maximum elongation and toughness presented by the SR700 specimen. In addition to this, it is still possible to eliminate the effect of the

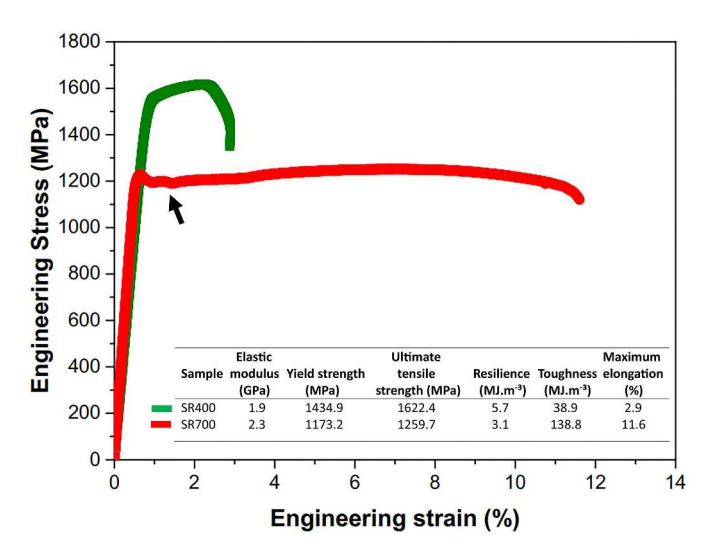


Fig. 4. - Engineering stress-Engineering strain curves obtained from tensile tests of SR400 and SR700 conditions. The black arrow indicates a discontinuous yielding behavior for the SR700 specimen under tensile deformation.

block size on the mechanical properties of both evaluated pearlitic conditions because the prior hot-rolling and patent treatment were carried out identically.

Another aspect to consider is that the elastic modulus of SR400 (1.9 GPa) and SR700 (2.3 GPa) were divergent. Under this subject, the elastic modulus of metals depends on their lattice constant. However, this parameter may be ignored by the fact that both conditions present the same crystalline structure in their matrix. In addition, the grain boundaries (grain size) and dislocation densities are other significant parameters that can degrade that elastic property by increasing the interaction distance between atoms located at the interfaces of these defects [43,44]. Based on this, Yu [45] demonstrated in their study that elastic modulus decreases with the increase of plastic strain. Therefore, the elastic modulus discrepancy observed between SR400 and SR700 may result from their difference in the amount of lattice defects (LABs and MABs), which may interfere in the average distance of their atomic interfaces. Additionally, a smooth behavior of discontinuous yielding was observed in the tensile-strain curve of the SR700 pearlitic specimen (as pointed out by a black arrow in Fig. 4). Many authors [35,46,47] reported that the release of locked dislocations in the Cottrell atmospheres causes this phenomenon. This is another indication that the carbon diffused to the dislocation zones during the stress relief treatment of SR700.

Furthermore, Fig. 5 and Fig. 6 reveal the potential θ/α ORs, respectively, for SR400 and SR700 pearlitic specimens acquired from the t-EBSD technique. In this case, it is possible to note in Fig. 5(f) that the $(001)_{\theta}$ ll $(\overline{11}0)_{\alpha}$, $(001)_{\theta}$ ll $(\overline{2}11)_{\alpha}$, and $(001)_{\theta}$ ll $(0\overline{1}1)_{\alpha}$

ORs detected in SR400 correspond to the Bagaryatskii OR:

 $[100]_{\theta}$ ll $[1\overline{10}]_{\alpha}$, $[010]_{\theta}$ ll $[111]_{\alpha}$, $(001)_{\theta}$ ll $(11\overline{2})_{\alpha}$ [48]. On the other hand, the $(031)_{\theta}$ ll $(0\ \overline{1}1)_{\alpha}$, and $(\overline{1}\ 03)_{\theta}$ ll $(101)_{\alpha}$ ORs identified in SR700 (see Fig. 6(f)) are equivalent to the Isaichev OR: $[010]_{\theta}$ ll $[111]_{\alpha}$ (103) $_{\theta}$ ll (01 $\overline{1})_{\alpha}$ [48]. In this context, some scholars [48,49] have reported that Isaichev OR was often considered an experimental error of Bagaryatskii OR. In addition to this, they have also mentioned the high difficulty of distinguishing these ORs via conventional electron diffraction techniques. This situation happens because the Bagaryatskii and Isaichev ORs present a few degrees of rotation (less than 4°) about their similar axis $[010]_{\theta}$ ll $[111]_{\alpha}$. Although this slight angular difference Zhou et al. [50] confirmed that the Bagaryatskii and Isaichev ORs have different cementite habit plans that match the same atomic plan of ferrite. Also, the authors indicated that the development of one of these ORs depends on the initially established interface at the pearlite nucleation onset. In view of this, some hypotheses about the ORs formation have been formulated from the literature. For instance, Dippenaar et al [51]

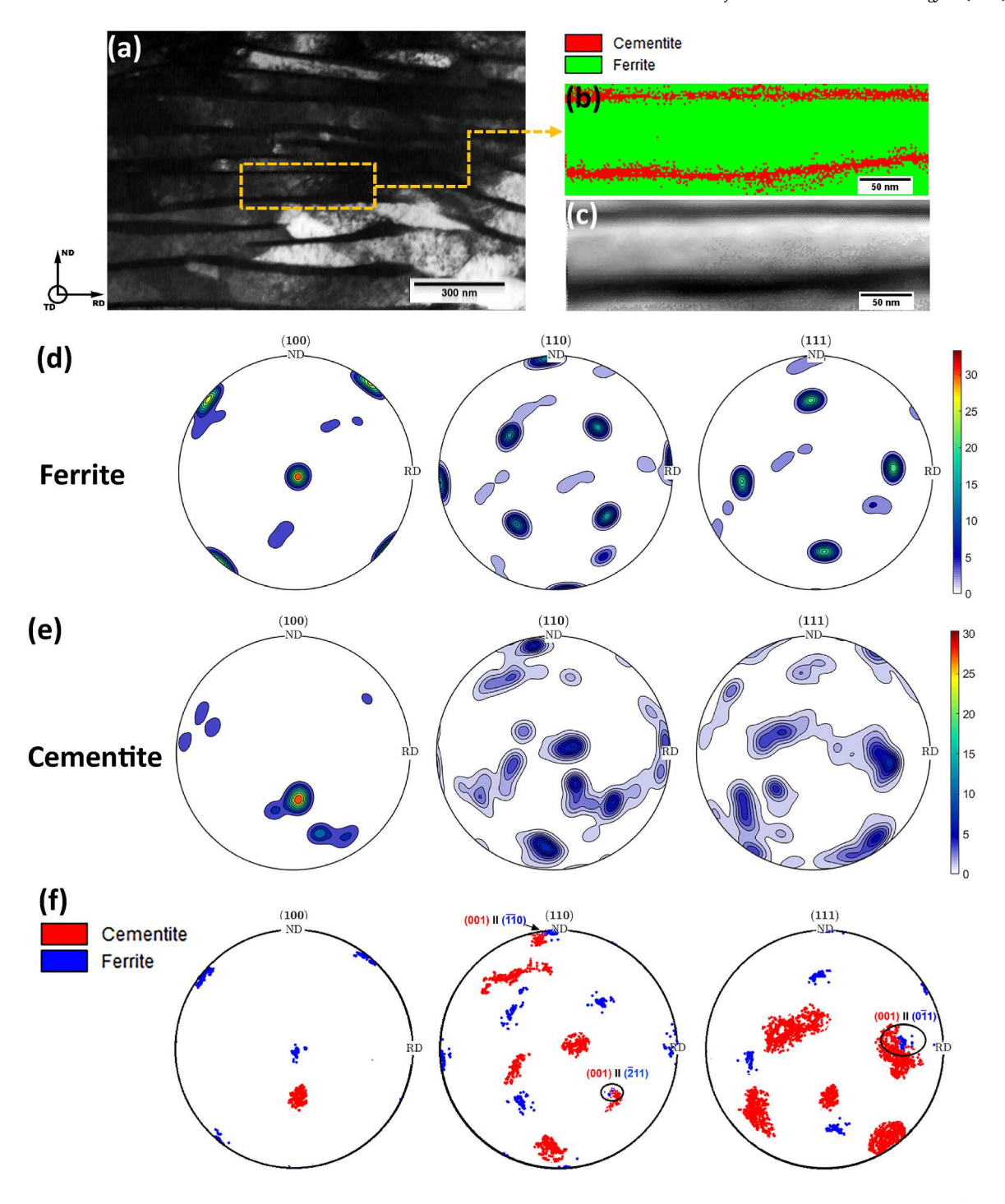


Fig. 5. Scanning transmission electron backscattered diffraction (*t*-EBSD) of SR400. **(a)** Scanning transmission electron microscopy bright field image of SR400 specimen. **(b)** Phases map of one region where the *t*-EBSD was performed in SR400. **(c)** Image quality map from the same *t*-EBSD area shown in (b). **(d)** (100), (110), and (111) pole figures of ferrite obtained from five *t*-EBSD maps in SR400. **(e)** (100), (110) and (111) pole figures of cementite obtained from five *t*-EBSD maps in SR400 **(f)** Overlapped (100), (110) and (111) pole figures from ferrite and cementite from the SR400's *t*-EBSD maps.

mentioned that the *Bagaryatskii* OR tends to be satisfied when pearlite nucleates from proeutectoid cementite in hypereutectoid steels. Conversely, the *Isaichev* OR is related to being settled when pearlites grow from proeutectoid ferrite, which usually happens in hypoeutectoid steels [52]. Moreover, Zhou et al. [50] confirmed in their experiment the presence of Isaichev OR in a hypoeutectoid steel. However, the authors found no *Bagaryatskii* OR in the hypereutectoid steel.

In this regard, once the stress relief treatment performed in SR400 (at a low temperature and short time) did not provide meaningful

microstructural changes, it is possible to consider that this thermal treatment may not have a significant effect on the SR400's θ/α OR. Therefore, it suggests that the *Bagaryatskii* OR was the θ/α OR in at least one condition before both stress relief treatments in the process route performed in the present research. So, the SR400's *Bagaryatskii* OR may have been developed in one or a combination of the preceding processes. However, it is quite difficult to determine where this SR400's OR was generated because the track of θ/α OR throughout the evaluated manufacturing route was not conducted in this work. Thus, this case

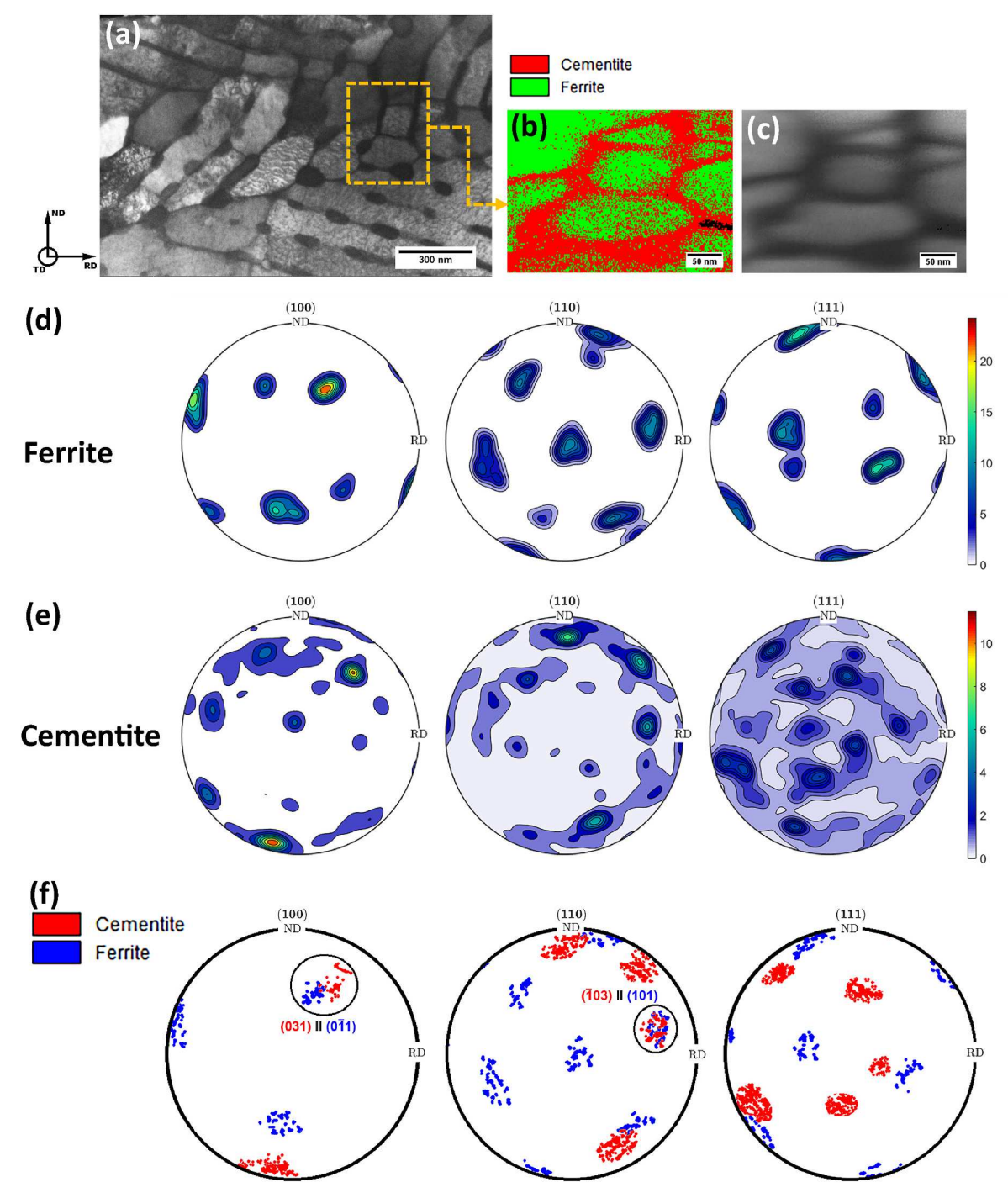


Fig. 6. Scanning transmission electron backscattered diffraction (*t*-EBSD) of SR700. **(a)** Scanning transmission electron microscopy bright field image of SR700 specimen. **(b)** Phases map of one region where the *t*-EBSD was performed in SR700. **(c)** Image quality map from the same *t*-EBSD area shown in (b). **(d)** (100), (110), and (111) pole figures of ferrite obtained from five *t*-EBSD maps in SR700. **(e)** (100), (110) and (111) pole figures of cementite obtained from five *t*-EBSD maps in SR700 **(f)** Overlapped (100), (110) and (111) pole figures of ferrite and cementite from the SR700's *t*-EBSD maps.

demands additional and accurate investigations. On the other hand, SR700 showed potential Isaichev OR together with a considerable microstructural modification, such as the partial cementite spheroidization that was accompanied by the mechanisms of carbon diffusion, coarsening, and decomposition. Based on this information, it is plausive to recognize that a new rearrangement of the cementite atoms (Isaichev OR) at the new cementite/ferrite interfaces produced during the partial cementite spheroidization may have taken place with a slight divergence from the prior lamellar structures (*Bagaryatskii* OR). Additionally, the mechanisms related to cementite redistribution, or the production of

new θ/α interfaces, occurred in an already stabilized ferrite structure during the partial spheroidization process that is analogous to the establishment of Isaichev OR in hypoeutectoid steels.

Therefore, the SR400 and SR700 pearlitic steel conditions, which are the starting point of the further in-situ TPB investigations, presented different cementite morphologies, discrepancies in the degree of defects in their ferritic matrixes, distinct mechanical properties, and a potential divergence in their cementite/ferrite ORs.

3.2. In-situ three-point bending (TPB) experiments and digital image correlation (DIC)

This topic focuses on designing the relationship between the mechanical performance and microstructural behavior of the SR400 and SR700 specimens during the introduction of four successive in-situ TPB experiments. In this context, Fig. 7 provides the load and elongation data acquired during the TPB analyses. More specifically, Fig. 7(a) and (b) exhibit the elongation-load curves plotted in a hysteresis shape for SR400 and SR700, respectively. In this case, the loops represent the cyclic bending alternation between the loading (B1 and B3) and reverse loading (B2 and B4), while the magnitude zero marked by the intersection of the two black dashed lines refers to the initial position of the loading pin. Regarding the elastic zones of the first bending (B1) in Fig. 7 (a) and (b) (indicated by black lines), they presented an elastic stiffness of 2.04 kN/mm for SR400 and 2.33 kN/mm for SR700. This result agrees with the elastic trend previously observed in the corresponding tensile test curves (in Fig. 4) of SR400 and SR700. Moreover, the episode of working hardening can be noticed in both B1 curves with the progress of the bending deformation. It means that both samples achieved the plastic region at the maximum preset elongation of 2.5 mm. Furthermore, it required a maximum load of 1638.6 N and 1558.3 N, respectively, for bending SR400 and SR700 up to 2.5 mm during B1. This outcome demonstrates again the tougher dislocation mobility in the lamellar pearlitic condition (SR400).

After that, the loading pin was displaced backward to the starting point, and the charge was released. At this moment, an elongation recovery occurred in both investigated pearlitic steel conditions. As a

result, the samples accompanied the return of the pin by keeping physical contact between them (loading pin and sample). However, the loading drop during the discharge events described an elastic restoration followed by an inelastic recovery that can be noticed in the amplified zones of Fig. 7(a) and (b). These magnified areas represent the unloading regions of B1 and B3 (indicated by red dashed rectangles). In this context, the deviation from Hooke's line may be an implication of microplastic strain caused by dislocation movement [53]. In this regard, it is pointed out from the literature [45,54-58] that this non-linear return after plastic deformation is usually attributed to the rearrangement of dislocations or damage. After B1, regarding the maximum elongation of 2.5 mm, the total elongation recovered for SR700 (around 0.71 mm) was a bit less pronounced than in SR400 (about 0.76 mm), which may be a consequence of their respective elastically recovered region that matches their corresponding initial elastic properties. On the other hand, the reverse plastic elongation (e_{rpe}) of the inelastic recovered zone was slightly higher for SR700 (around 0.13 mm) in relation to the e_{rpe} of SR400 (around 0.10 mm). In view of this, it has been reported that the reverse plastic strain has a straight relationship with the intensity of the Bauschinger effect [58]. The Bauschinger effect is characterized by a softening response of the material under cyclic conditions due to the reverse change in the loading path.

Then, after resetting the rectangular sample's position by putting the surface that was in contact with the loading pin for touching the support pins, the reverse bent (B2) was introduced in the samples just after the B1's unloading stage. In this regard, the initial position of the following bending (B2) in SR400 started around the point where the inelastic recovery effect ceased, which was about 1.74 mm. Conversely, this

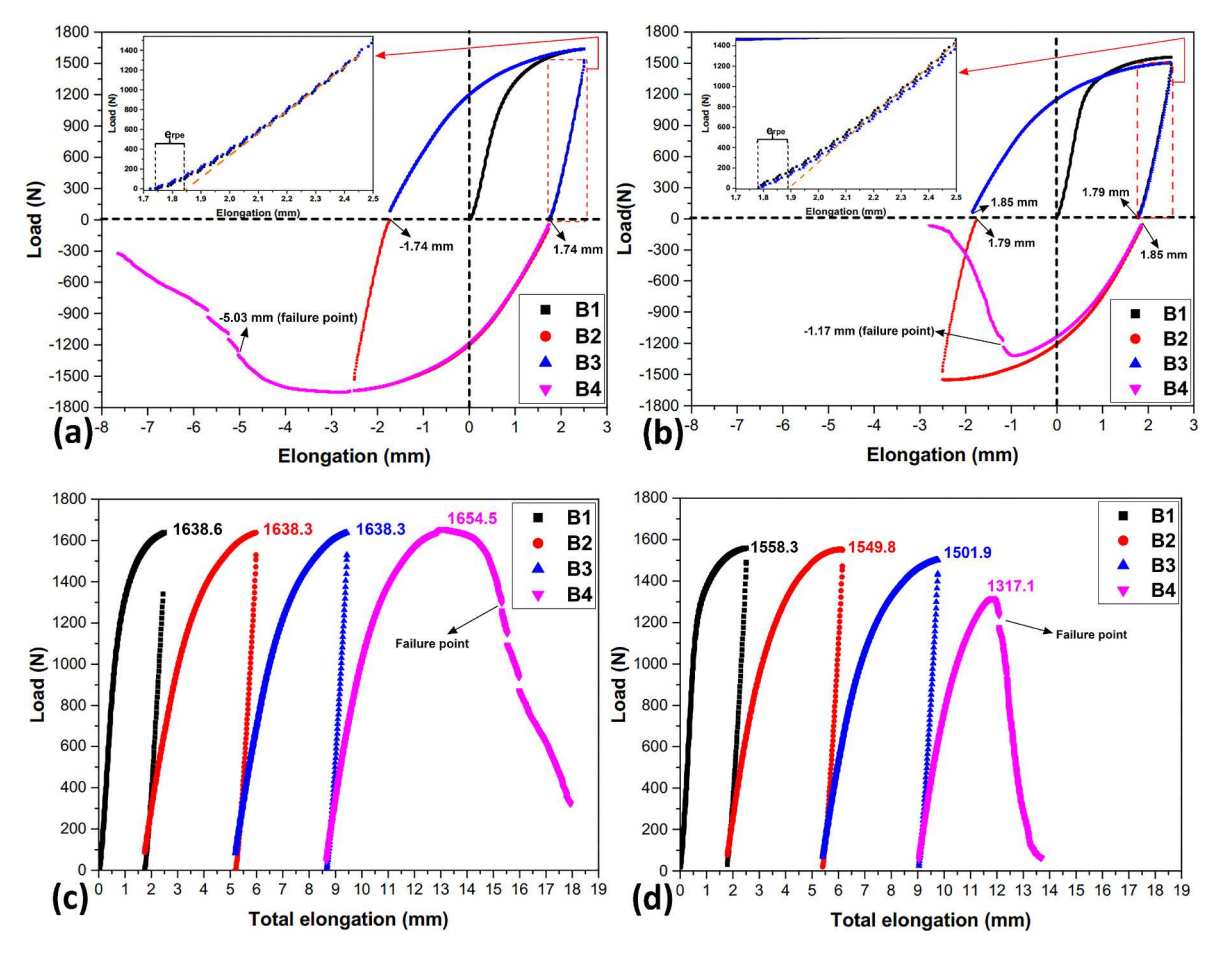


Fig. 7. Elongation-load hysteresis curves obtained during the cyclic in-situ three-point bending (TPB) test for **(a)** SR400 and **(b)** SR700 pearlitic steel conditions. Total elongation-load plotted from Elongation-load hysteresis data obtained during the in-situ cyclic TPB experiment for **(c)** SR400 and **(d)** SR700 specimens. In **(a)** and **(b)**, e_{rpe} means reverse plastic elongation.

behavior did not occur for SR700. Instead, the start point of B2 in SR700 was greater (1.85 mm) than the final location (1.79 mm) of its B1 discharge step. This phenomenon was a consequence of the slippage of the SR700 specimen when the loading pin touched its surface. So, it may likely be due to the weaker strength of SR700. Likewise, these transition patterns detected between B1 and B2 were also observed during the further shift steps between the succeeding bending (B2/B3 and B3/B4) for both conditions (SR400 and SR700). Moreover, the resultant elongation-load curves of B2, B3, and B4 developed an almost parabolic behavior that seems to have a small elastic region and a predominant hardening zone. Furthermore, it is possible to realize that the

phenomenon of restoration still happened during the other discharge stages (after B2 and B3) in both investigated conditions. In addition, it is interesting to note that SR400 provides a symmetric hysteresis pattern while SR700 does not. In view of this, the loading, in positive values, was plotted against the total elongation undergone by each sample throughout the four-succeeding bending procedures, as shown in Fig. 7 (c) for SR400 and Fig. 7(d) for SR700. Based on this, there is a continuous trend of softening (Bauschinger effect) throughout the progress of the four-bending applied in SR700. This event suggests that the SR700 may be susceptible to the rearrangement and annihilation of dislocation, probably due to the inferior number of obstacles available in its

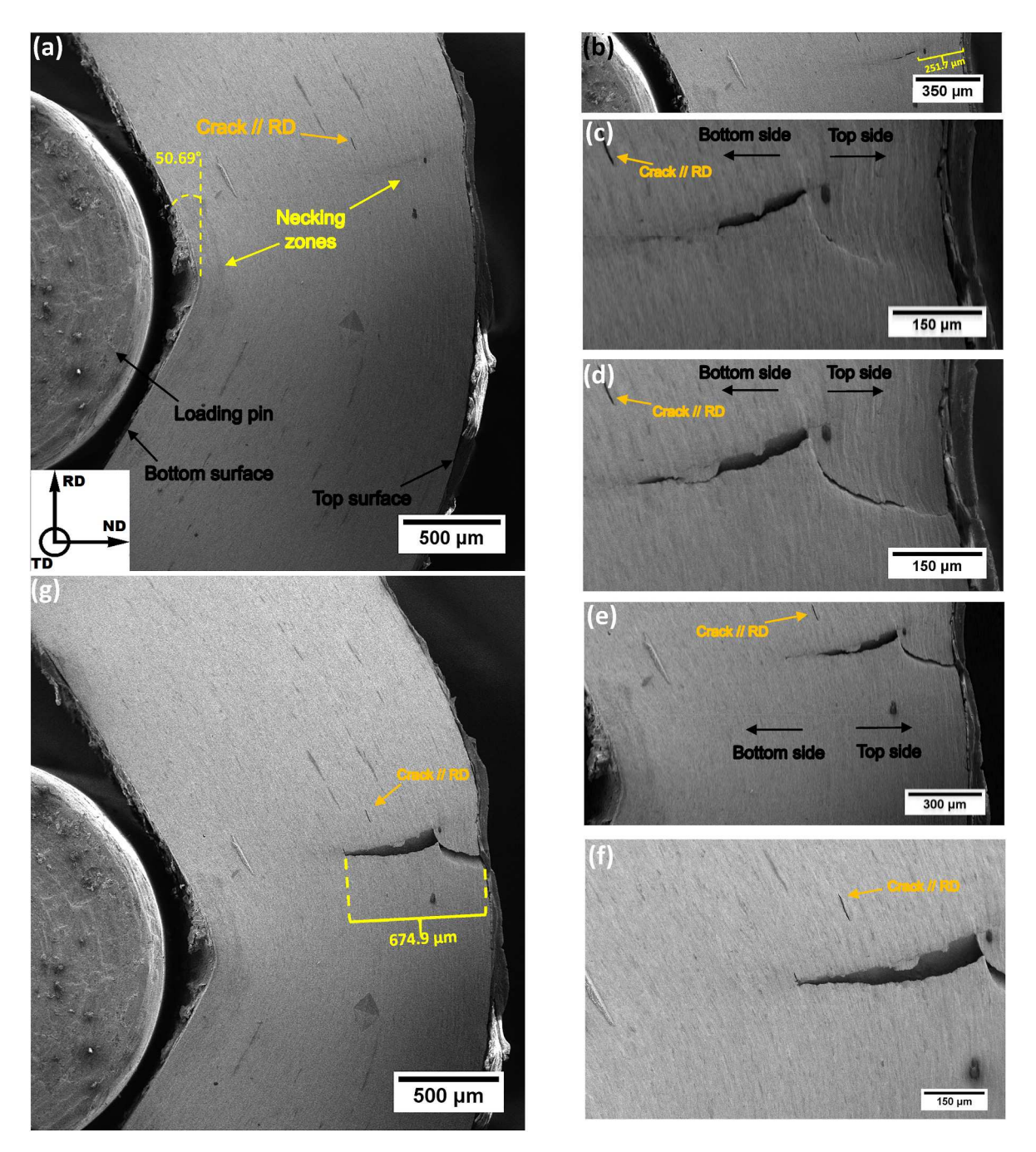


Fig. 8. Macro scanning electron microscope (SEM) images around the moment the crack achieved the lateral surface (RD - ND) of the SR400 specimen during the fourth successive in-situ three-point bending test: (a) Just before the crack arrived on the lateral surface (RD - ND), (b) At the moment the crack arrives on the lateral surface (RD - ND), (c) Just after the crack arrived on the lateral surface (RD - ND), (d) (e) Different instants of the crack propagation throughout the specimen's thickness (about the ND direction), (f) At the moment the crack stopped to propagate throughout the specimen's thickness (about the ND direction) in higher magnification, and (g) Final lateral crack in a lower magnification.

microstructure for avoiding dislocation gliding in addition to microstructural heterogeneity (small recrystallized grains). Otherwise, SR400 showed a balanced mechanical performance during the four TPB experiments with a slight hardening in the last bending phase (B4). In this case, the almost constant mechanical behavior of SR400 evidences the high stability of the lamellar pearlitic microstructure that inhibits the plastic flow in the ferritic matrix like a reinforcement grid. These microstructural effects on the bending mechanical performance of

SR400 and SR700 also corroborate with their maximum failing elongation, which was 5.03 mm for SR400 and just 1.17 mm for SR700 during the last bending procedure (B4). In summary, this fact reinforces the higher microstructural stability of SR400 about SR700 for damage onset.

Furthermore, the first nucleated cracks at the failure point of SR400 (at 5.03 mm) and SR700 (at 1.17 mm) could not be recorded during the in situ B4 step. Unfortunately, the initial cracks were nucleated on the

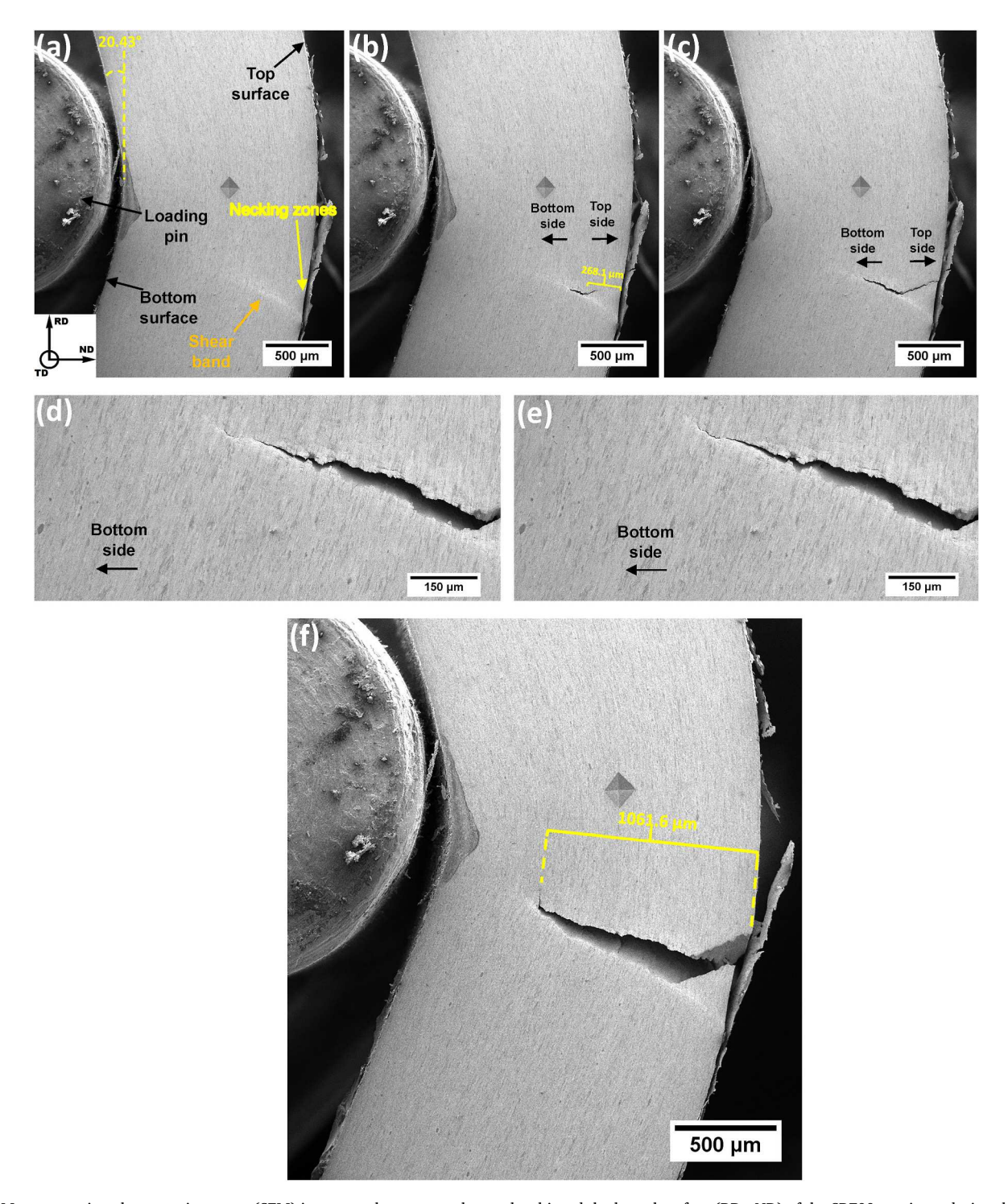


Fig. 9. Macro scanning electron microscope (SEM) images at the moment the crack achieved the lateral surface (RD - ND) of the SR700 specimen during the fourth successive in-situ three-point bending test: (a) Just before the crack arrived on the lateral surface (RD - ND), (b) At the moment the crack arrives on the lateral surface (RD - ND), (c) Just after the crack arrived on the lateral surface (RD - ND), (d) (e) Different instants of the crack propagation throughout the specimen's thickness (about the ND direction), and (f) Final lateral crack.

outer top surfaces (TD - RD) under a tensile state. This event was also reported by Arola et al. [28] and Saastamoinen et al. [27] These authors have observed a similar position of crack nucleation on rectangular steel samples under TPB conditions. After nucleation, the flaws propagated predominantly into the TD direction up to find the samples' lateral section (ND - RD). In this way, the cracks arrived on the ND - RD surface quickly, which means immediately after the specimens' failure. Then, the fracture grew essentially throughout the specimen's thickness (around ND direction). So, Fig. 8 and Fig. 9 exhibit the macro view of the exact moment the cracks achieved the lateral section (ND - RD) of SR400 and SR700, respectively. The references of the top and bottom surfaces are exhibited in Fig. 2(b). Regarding the SR400 condition, Fig. 8(a) shows the ND - RD lateral surface at the failure instant (at 5.03 mm). In this regard, it can be noticed two local necking zones pointed out by two yellow arrows in Fig. 8(a), one in the top area (located almost below the loading pin lateral) and another near the bottom surface (just below the loading pin center). This situation suggests the SR400 condition underwent a severe local plastic deformation before its failure. In addition to this, the deflection angle of SR400 was around 50.69° at the failure point. In this case, the crack reached a location on the lateral section (ND - RD) 251.7 µm below the top surface and near the necking zone (Fig. 8) (b)). This fact may result from a structural stress relief in this edge volume as the initial crack propagated into the TD and ND directions. Next, the defect grew, at the same time, into the bottom (compressed region) and the top (area under tensile) sides (Fig. 8(c), (d), and Fig. 8

In this regard, the failure propagation into the top side presented some deviations. In this case, it first propagated into the RD direction, then shifted into a diagonal path until it arrived on the top surface. This phenomenon may occur due to the structural stress relaxation in the edge zone. Based on this, the fracture may lose part of its driving force to grow into this region. Therefore, pearlitic blocks stretched into the RD direction with lamellae cementite may have initially held this crack propagation as a barrier. As a result, it kept the fracture progress in the RD direction until it found a region prone to crack growth, such as shear bands. Many researchers [27,28,59,60] have confirmed the formation of shear bands in regions near the external surface of the specimen under tensile stress during TPB experiments. Then, the failure developed and reached the top surface by following a tilted shear band-like profile. On the other hand, concerning the behavior of the break going into the bottom side, the fracture tended to be almost perpendicular to the sample's external surfaces (top or bottom). This behavior may be a consequence of the tensile stress components that are arranged around the same direction of the sample's outer surfaces. Thus, the tensile components act by opening the crack. Also, Fig. 8(f) and (g) indicate that the fracture depth from the top surface was $674.9~\mu m$ in the SR400 condition. Moreover, it is interesting to note that the final crack tip changed to the RD direction. This fact suggests the effect of the pearlitic blocks stretched into the RD direction that may stabilize the defect propagation. In this setting, it is also possible to observe in Fig. 8 (indicated by orange arrows) a stable crack parallel to the RD direction that did not change in length during the failure progress due to its parallel arrangement about the tensile component. Additionally, the neighbor pearlite colonies, with their set of lamellae in divergent directions, may help to inhibit this crack growth.

Concerning the SR700 condition, Fig. 9(a) displays the lateral surface (ND – RD) at the SR700's failure instant. At this moment, a very small necking zone was observed, indicated by a yellow arrow in Fig. 9 (a). Moreover, a long shear band can be seen as the brighter line near the necking area of SR700 (pointed out by an orange arrow). This shear band was formed in the top region (under tensile stress) and situated in a zone almost below the loading pin lateral. Moreover, the deflection angle at the failure of the SR700 was only 20.47° , which is smaller than in the SR400 condition. In Fig. 9(b), it is possible to realize that the crack achieved the lateral surface (ND - RD) precisely in the macro shear band zone. Moreover, the break found the SR700's ND - RD lateral, $268.1~\mu m$

below the top surface. Likewise, in SR400, this event may also happen due to the structural stress relief in the edge region as the crack grew into the TD and ND directions. After arriving on the SR700's lateral surface, the fracture had the same behavior as in the SR400 condition by spreading at the same time into the bottom and the top sides (Fig. 9(c), (d), and Fig. 9(e)). However, the SR700's defect propagated faster than in the SR400 condition. Moreover, the SR700's crack provided a similar profile to the defect found in the SR400 specimen. Otherwise, no traces of crack growth restriction in the shape of SR700's fracture were observed. Therefore, the exact mechanisms related to the fracture propagation of SR400 may also be considered for the SR700 condition, but with lesser barriers against the crack growth due to SR700's non-lamellar pearlitic architecture. As a result, the total fracture depth in the SR700 specimen was 1061.6 µm from the top surface (Fig. 9(f)).

Based on the bending failure behavior of SR400 and SR700, it is plausible to acknowledge that the region in the top zone of the samples located nearly below the lateral of the loading pin is prone to strain concentration. In this case, it may be a consequence of the combined effect of the moment and stress gradient distributions, respectively, throughout the length and thickness of the specimens [26,28]. Moreover, the different features of crack propagation between the SR400 and the SR700 reveal the significant influence of the cementite morphology since both evaluated conditions have the same profiled stretched pearlitic blocks. Furthermore, these observations confirm that the lamellar pearlitic architecture tends to retard the macro shear band development and damage initiation, as mentioned by Kapp et al. [26].

Additionally, Fig. 10 and Fig. 11 present, respectively, for SR400 and SR700, the microstructural behavior on their top and bottom regions during the first three consecutive TPB experiments. These evaluated zones were situated just below the middle point of the loading pin. In detail, the magnified central regions of Fig. 10(a), (b), Fig. 11(a), and Fig. 11(b) (marked by dashed yellow rectangles) confirm that the cementite morphology before the bending deformation on the top and bottom zones is lamellar for SR400 and partially spheroidized for SR700. Concerning the microstructural behavior between the bending steps, it is difficult to realize how the microstructure was changed in Figs. 10 and 11. However, the pearlitic microstructures were, in general, slightly stretched into RD and contracted into ND directions when they were located on the opposite side of the loading pin, for example, on the top regions of B2 (Figs. 10(e) and Fig. 11(e)) and bottom regions of B1 (Figs. 10(d) and Fig. 11(d)) and B3 (Figs. 10(h) and Fig. 11(h)). On the other hand, the microstructures were elongated in ND and compressed in RD when they were situated on the same side of the loading pin, for instance, on the bottom zones of B2 (Figs. 10(f) and Fig. 11(f)) and top zones of B1 (Figs. 10(c) and Fig. 11(c)) and B3 (Figs. 10(g) and Fig. 11 (g)). Furthermore, it was realized that the microstructures underwent small rotations mainly during the B3, likely due to the deformation mechanism of shear bands. In this context, the detected local regions where a microstructural sliding was noticed (shear bands) are pointed out by yellow and red arrows in Fig. 10(g), (h), Fig. 11(g), and Fig. 11 (h). Again, these slight displacements are tough to be noticed. Based on this, it was included in Fig. 10(i), (j), Fig. 11(i), and Fig. 11(j), the resultant Eulerian strain (e_{yy}) maps obtained via DIC from the first three subsequent bending procedures. The areas assessed by DIC are marked by dashed orange rectangles in Fig. 10(g), (h), Fig. 11(g), and Fig. 11(h). In this way, the local strain visualization is easier to be noticed in the e_{vv}

So, it can be seen in Figs. 10(j) and Fig. 11(j) positive strain values due to the tensile stress component lengthening the microstructure in the y-axis. Conversely, the negative strain values in Figs. 10(i) and Fig. 11(i) express the effect of the compressive stress that squeezes the microstructure in the y-axis. Moreover, the profile of the higher local strained regions in the e_{yy} maps seems to be concentrated in lines aligned around 45° about the ND. In addition, the higher strained areas shown in the Eulerian strain maps matched the local slid zones (shear bands) found inside the orange rectangles on the SE images. In this

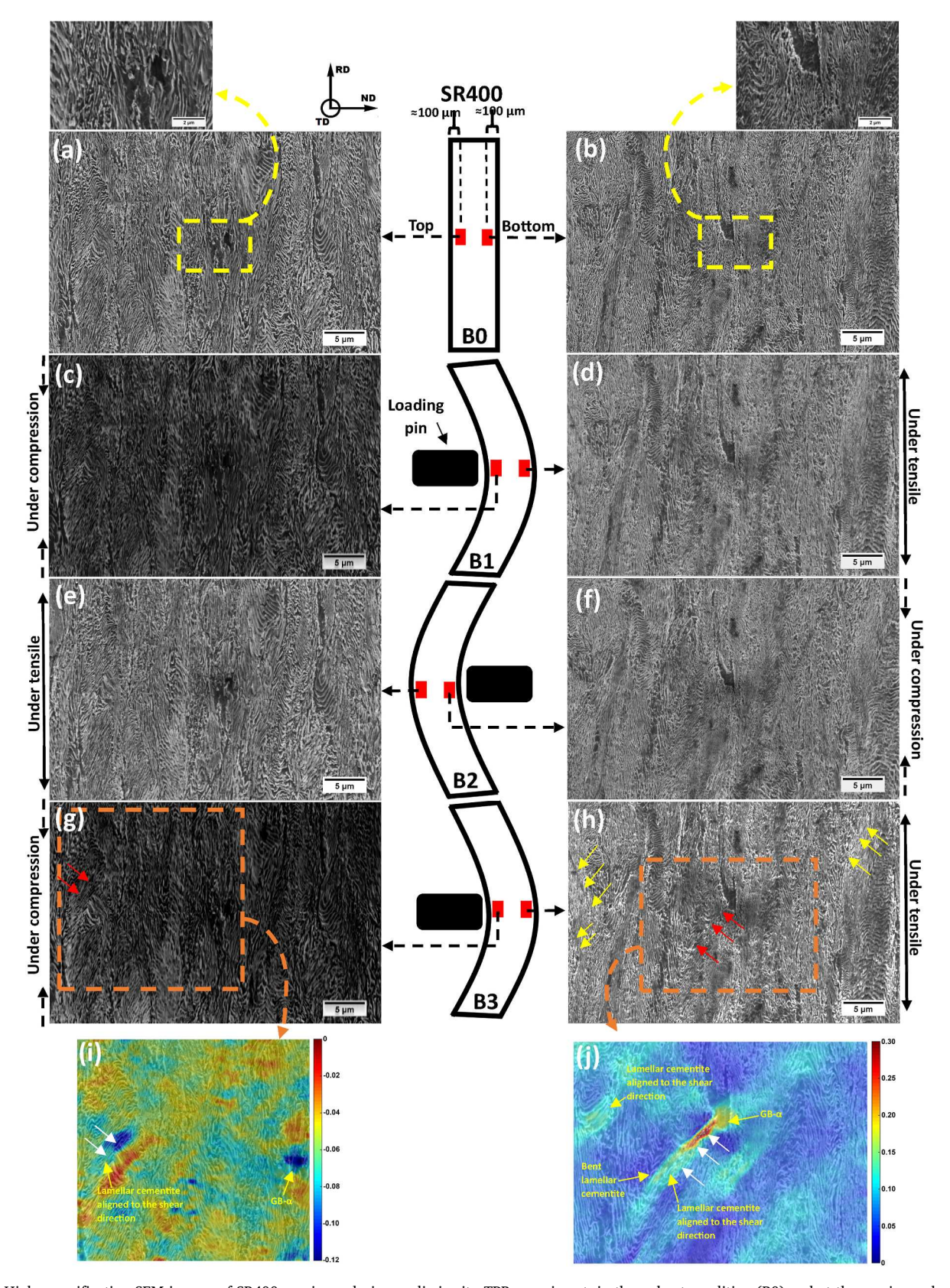


Fig. 10. High magnification SEM images of SR400 specimen during cyclic in-situ TPB experiment, in the unbent condition (B0) and at the maximum loading pin displacement (2.5 mm) during B1, B2 and B3, respectively, for the two constant evaluated specimen's regions: 10 nm below the (a) (c) (e) (g) top and 10 nm above the (b) (d) (f) (h) bottom. (i) (j) Eulerian strain maps, e_{yy}, obtained via digital image correlation (DIC) from the area marked by orange dashed rectangles in (g) and (h) during the first three subsequent bending procedures.

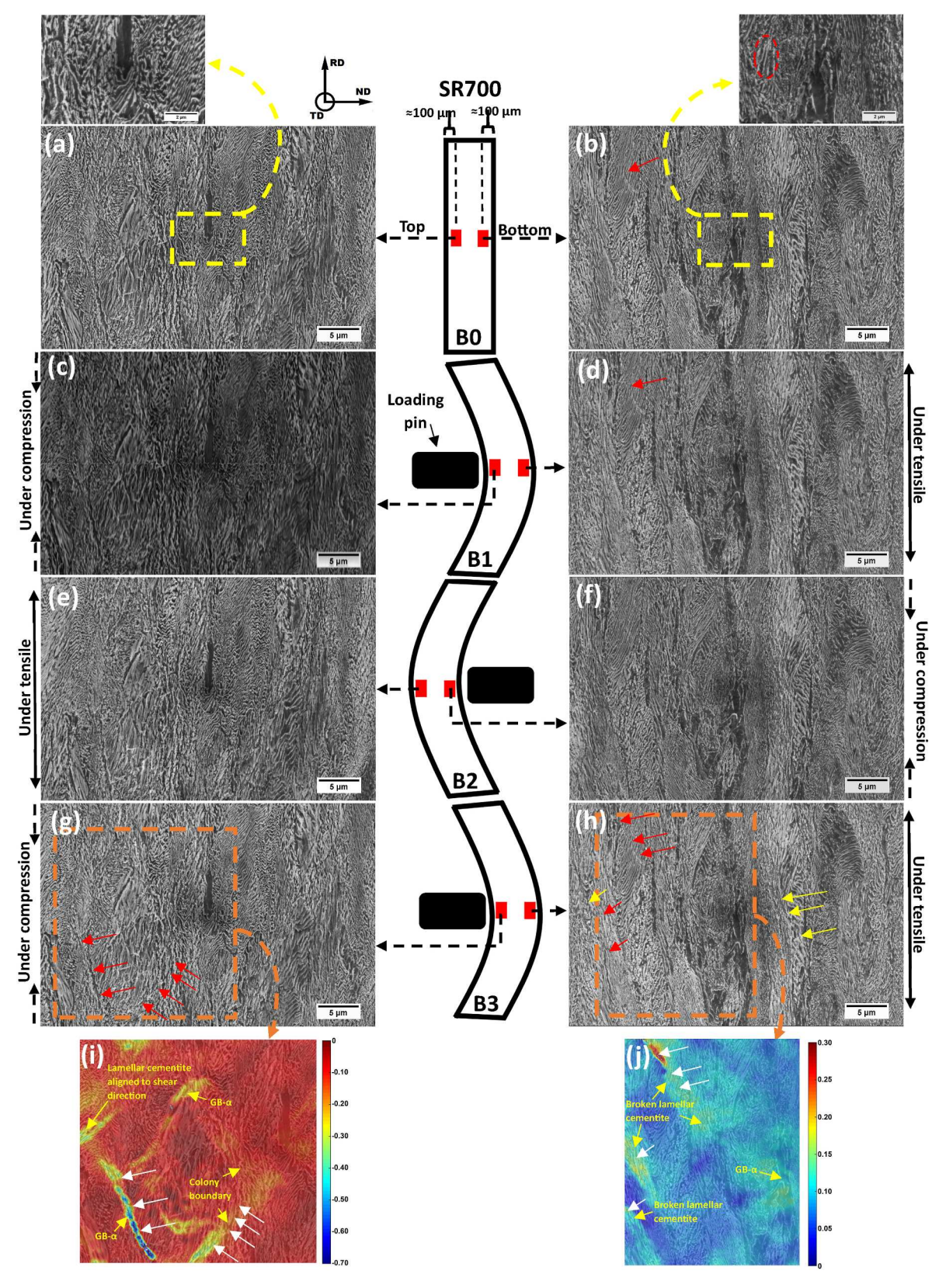


Fig. 11. High magnification SEM images of SR700 specimen during cyclic in-situ TPB experiment, in the unbent condition (B0) and at the maximum loading pin displacement (2.5 mm) during B1, B2 and B3, respectively, for the two constant evaluated specimen's regions: 10 nm below the (a) (c) (e) (g) top and 10 nm above the (b) (d) (f) (h) bottom. (i) (j) Eulerian strain maps, e_{yy}, obtained via digital image correlation (DIC) from the area marked by orange dashed rectangles in (g) and (h) during the first three subsequent bending procedures.

scenario, the equivalent regions of shear bands are pointed out by red arrows in the SE images and white arrows in the e_{yy} maps. Thus, these outcomes may confirm the strain concentration inside shear bands and their formation on both border regions (top and bottom) during the third successive bending procedure. More specifically, Fig. 10(g), (h), Fig. 10 (i), and Fig. 10(j) display the higher strains (e_{yy}) values in the top (around -0.12) and bottom (in the range of 0.17-0.30) areas of SR400 during B3 were located near or inside ferritic grain boundaries (GB- α), bent lamellar cementite and colonies with lamellar cementite orientation aligned to the shear direction (as indicated by yellow arrows in Fig. 10(i) and (j)).

Regarding SR700, Fig. 11(h) and (j) show, in the bottom zone, that the higher strain values (around 0.17-0.30) are mainly concentrated around the broken cementite lamellae. This result suggests that the remaining lamellae of cementite in SR700 are brittle. This phenomenon may result from a partial cementite dissolution into the ferrite matrix. Consequently, holes can be produced throughout the cementite lamellae, as indicated by a red dashed circle in the amplified zone of Fig. 11(b). In this case, these holes may concentrate stress when the lamellae are submitted to the external effort, and consequently, they are easily broken. In addition, the region with fractured lamellae cementite, situated higher up within Fig. 11(h), is presented in Fig. 11(b) (indicated by a red arrow) before the bending deformations, which means in the stress-relieved condition at 700 °C. In this stage, some cementite lamellae were already disconnected, while others were still linked but bent. These features are similar to the previously presented shear band zones in Fig. 3. Therefore, this region seems to indicate a prior shear band that was formed during the cold rolling process, which then was partially spheroidized (disconnected region) after the stress relief treatment at 700 °C. Next, Fig. 11(d) shows that the bent lamellae are easily fractured (pointed out by a red arrow) under the tensile stress caused by the first bending (B1). This event insinuates again a lamellae cementite embrittlement after the stress relief at 700 °C. Thus, in addition to cementite lamellae fragilization, it is also reasonable to consider that after undergoing a stress relief treatment at a high temperature (700 °C), the shear bands introduced during the prior cold rolling process become regions prone to strain concentration under the TPB state.

Furthermore, the overall highest value of strain (-0.70) was found in the SR700's top zone during B3 (see Fig. 11(i)). In this case, the strain was concentrated in an elongated GB- α area aligned about the shearing direction. In view of this, the combination of factors in this specific region together with the microstructure of the SR700 may have contributed to this highest local strain concentration: partially spheroidized and brittle cementite, lack of barriers in the GB- α against dislocation slippage, and easier alignment of the GB- α length for dislocation motion (just like in lamellae of pearlites aligned into the shear direction). Still, in this setting, the boundary of a pearlitic colony also accumulated a considerable degree of strain (around -0.25), as shown in Fig. 11(i). In this instance, it was seen that this specific pearlitic colony rotated more than its neighborhood area. This may indicate a possible initial phenomenon of decohesion between the pearlitic colony due to the malleable behavior of SR700's microstructure in addition to the anisotropic colonies' deformability [61]. This event agrees with a recent work [62] that identified via an in-situ SEM experiment that pearlitic colony decohesion can occur in soft pearlitic microstructure under shear deformation. In addition, the researchers showed that the fracture propagation passed through the pearlitic colony boundary where decohesion occurred. Therefore, it demonstrated a potential interface for crack nucleation in SR700. Based on these results, it is reasonable to state that the rectangular SR400 specimen has a solid and balanced microstructural behavior on its near border regions during the cyclic bending deformations. Otherwise, SR700 does not.

3.3. Electron backscattered (EBSD) in interrupted three-point bending (TPB) experiments

The current section centers attention on providing supplemental information about the behavior of lattice strain after each of the four consecutive bending procedures applied in the two evaluated pearlitic steel conditions. Based on this, the plastic strain investigation was conducted by tracking the diffraction patterns degradation (image quality intensity) from a determined EBSD area evaluated after consecutive interruptions of the TPB cycles (After B1, After B2, After B3, and During B4). In this context, the image quality (IQ) is strongly affected by residual strains in the microstructure, and therefore, indirect interpretations of lattice defects, such as dislocations, can be drawn. In this way, the IQ data can be plotted in a gray contrast map where the higher deformed regions (high dislocation density) are darker and under low intensities of IQ (degraded pattern quality) [63].

Fig. 12 displays the inverse pole figure (IPF) and their IQ maps of SR400 and SR700 conditions obtained from the interrupted bending tests. The analyzed areas were situated 100 nm below the top surface. Moreover, the IQ intensities were extracted and tracked from the invariable areas delimited by yellow dashed rectangles in Fig. 12(b) and (d). These constant areas were defined because of the physical distortion of the microstructure during the bending deformations. The averages of the IQ intensities for each specimen and bending condition were plotted in Fig. 13. Based on this, initially in B0 (stress-relieved condition), it is possible to observe that there is a slight difference between the IQ averages of SR400 (127.4) and SR700 (131.7). In this case, SR700 has a great value or better pattern of IQ than SR400. This IQ divergence agrees with the shorter length of LABs and MABs (lattice imperfections) previously detected in SR700 about the SR400 (see Fig. 3). So, After B1 and After B2, the pattern quality tended to decrease in both samples, which means that the amount of lattice defects increased during the two first bending deformations. However, it is interesting to note that the rate of IQ reduction is higher in the SR700 than in the SR400 condition. In this context, the partial spheroidization of cementite increases the total length of the θ/α interfaces in the SR700 specimen, where are the primary sources for dislocation nucleation in pearlitic steels [21,41]. In addition to the total length of θ/α interfaces, the degree of atomic mismatch at the θ/α interface affects the dislocation generation during plastic deformation [48,64]. However, there is just a slight angular difference between the orientation relationships found in SR400 (Bagaryatskii) and SR700 (Isaichev). Therefore, it demands additional and accurate investigations to prove distinctions between the Bagaryatskii and Isaichev ORs as a source for dislocation nucleation.

Conversely, there was a recovery of the pattern quality for both evaluated specimens (as marked by a green dashed circle in Fig. 13) in the After B3 bending condition. This event may be related to the annihilation of dislocations [58]. In this case, the image quality restoration was higher for SR700 than SR400. This potential higher dislocation annihilation in SR700 may result from its ineffective impediment for dislocation motion due to its non-entirely lamellar cementite morphology. In this case, dislocations have more freedom to move and interact with dislocations in the neighbor ferritic lamellae. Consequently, it may increase the probability of opposite signals dislocations meet and annihilate each other [41,58,65].

Furthermore, SR700 failed at 1.17 mm during B4. Regarding the interrupted EBSD analyses, this failed elongation (1.17 mm) was taken as a reference and set as the maximum elongation for SR400 during its B4 step. Therefore, this bending standard enables the comparison between SR400 (no failed) and SR700 (failed) under the same bending circumstances (During B4). In view of this, Fig. 13 shows that the IQ intensity started to decrease again during the fourth bending condition (During B4) for both investigated samples. In this instance, SR700

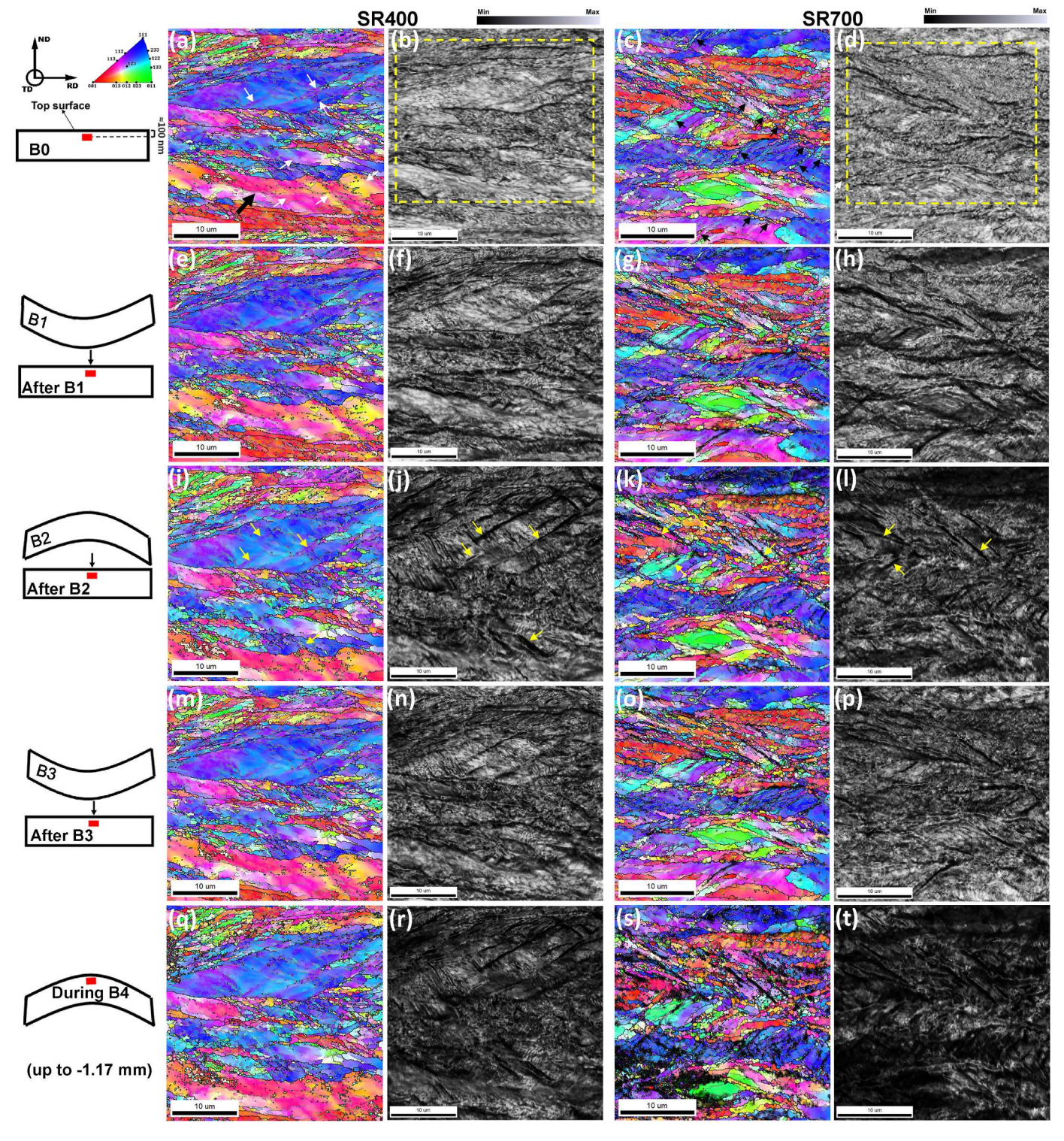


Fig. 12. Color-coded inverse pole figure (IPF) map and image quality (IQ) map, respectively, in the interrupted TPB condition of: (a) (b) unbent condition (B0), (e) (f) After B1, (i) (j) After B2, (m) (n) After B3, and (q) (r) During B4 for SR400 specimen, and (e) (d) unbent condition (B0), (g) (h) After B1, (k) (l) After B2, (o) (p) After B3, and (s) (t) During B4 for SR700 specimen. The big black and the small white arrows in (a) indicate the mostly violet big pearlitic block with many small bad indexed regions and shear bands, respectively. The small black arrows in (g) indicate zones with many small ferritic grains. The yellow dashed rectangles in (b) and (d) show the reference areas for both evaluated specimens, where the image quality intensities were acquired for all TBP steps. The small yellow arrows in (i), (j), (k), and (l) indicate the matched regions between the IPF and IQ maps.

achieved the lowest IQ intensity. This indicates again a greater rate of defect formation in the partially spheroidized pearlitic specimen.

In general, the IQ maps presented in Fig. 13 suggest that the SR700 has a higher capacity for generating and eliminating dislocations than the SR400 specimen concerning cyclic bending events. In this way, it

confirms, again, the microstructural stability of SR400. In particular, it was noticed that the improvement of IQ intensity in the two studied specimens happened only in the After B3 bending step. Under this circumstance, the EBSD areas were evaluated after being submitted to a compression stress state. This situation may suggest that the compressed

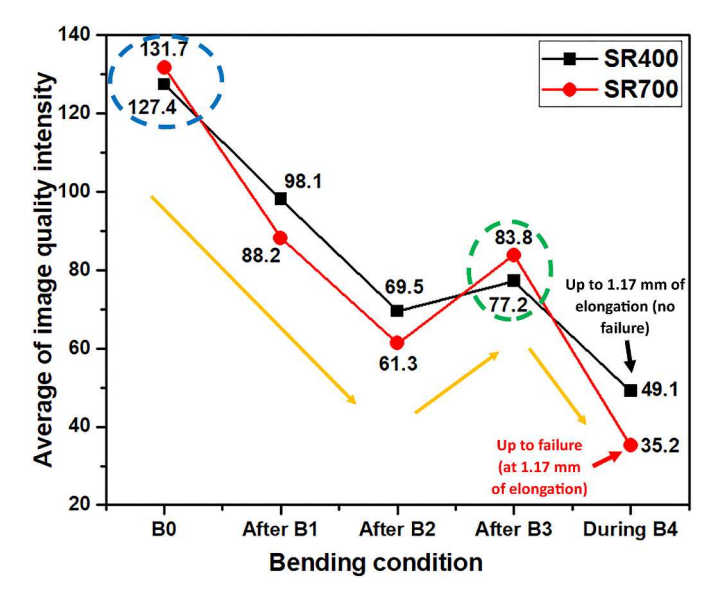


Fig. 13. Average image quality (IQ) intensity vs. bending condition during the interrupted three-point bending operation for SR400 and SR700. The IQ intensities were obtained from the image quality maps in on the delimited areas indicated by yellow dashed rectangles in (b) and (d).

region under cyclic bending deformation is more susceptible to the phenomenon of dislocation annihilation. However, it did not happen in the After B1 conditions, which were also evaluated just after a compressive step. In this case, it may imply that the amount of defect distributed in the ferritic matrix was not enough to enable the occurrence of interaction between dislocations of opposite signals. Therefore, in addition to the compressive state, the different trend between the IQ data of After B1 and After B3 suggests that a minimum amount of lattice defects is required for starting the destructive interaction among opposite signal dislocations.

Moreover, regarding the mechanical behavior of SR400 and SR700 in Fig. 7, it is reasonable to consider that the lamellar pearlitic condition (SR400) is less sensitive to the divergence of lattice defects (IQ intensity). This means that the variation of crystallographic imperfection during B1, B2, and B3 was not enough to cause any strain hardening during the three first successive bending experiments in the SR400 specimen, once more demonstrating its microstructural stability. Otherwise, it is possible to recognize that the Bauschinger effect in the SR700 indicates a significant dependence of the SR700's mechanical performance on its set of lattice irregularities during the cyclic bending procedure. Based on this, SR700 had a short but considerable maximum loading reduction from B1 to B2. At the same time, the IQ average of SR700 also decreased from After B1 to After B2 (see Fig. 13). In this scenario, the reverse loading path applied during B2, together with the no effective cementite obstacles in SR700, may have led to the redistribution of dislocations from pill-ups and tangles created during B1. Meanwhile, more dislocations were introduced into the SR700's ferritic matrix during B2 due to the IQ reduction in After B2 condition. As a result, the maximum charge was reduced by only 8.5 N from B1 (1558.3 N) to B2 (1549.8 N). Then, a more significant reduction in the maximum loading (47.9 N) was observed in SR700 from B2 (1549.8 N) to B3 (1501.9 N). In this case, as the IQ average increased from After B2 to After B3, the B3's softening was likely due to the annihilation of dislocations. Finally, the highest abrupt lowering in the loading (184.8 N) was observed in SR700 from B3 (1501.9 N) to B4 (1317.1 N), followed by failure (at 1.17 mm of B4), insinuating a possible microstructural damage influence.

More specifically, the IPF maps, shown in Fig. 12, were acquired with a square grid geometry. This grid type usually has a lower resolution for EBSD data indexation in relation to the hexagonal one. So, this can

generate some local incorrect index extrapolations [66]. For instance, the large pearlitic block (mostly in violet color) indicated by a big black arrow in Fig. 12(a) has many small grains that may result from the unsuitable indexation. Despite this inconvenience, it can be realized some evidence of shear bands in the SR400 that are pointed out by small white arrows in the IPF map (Fig. 12(a)). Otherwise, the same shear band feature was not identified in the SR700 (Fig. 12(c)). Instead, despite the mentioned problem for EBSD data indexation, many possible small grains were observed in Fig. 12(c), and small black arrows indicate some of them. In this case, the potential small grains are aligned in profiles similar to shear band patterns identified in Fig. 3(d), which supports a potential proper indexation of these small-scaled areas.

Moreover, it can be noticed that the darker regions (higher strained area) of the IQ maps during the progress of the cyclic bending were concentrated mainly in the shear bands and small grains zones, respectively, for the SR400 and SR700 conditions. For example, Fig. 12 (i) and (j) exhibited some corresponding regions (marked by yellow arrows) of shear bands and deformed zones for SR400, Likewise, Fig. 12 (k) and (l) displayed equivalent regions of small aligned grains and strained areas (also identified by yellow arrows) in SR700. In this context, Zhao et al. [65] presented in their work, via transmission electron microscopy micrographs, the behavior of dislocations inside a shear band in a lamellar pearlitic steel. Based on this research, the dislocations were piled up at the θ/α interfaces, and consequently, the cementite lamellae were bent due to their plasticity. Then, when the strain was large enough, the cementite lamellae broke, and the flow of dislocations continued into the neighbor ferritic lamella, which allowed the interaction between more dislocations. Finally, the softening mechanism may occur due to the annihilation of dislocations. Therefore, the deformation mechanism via shear band in lamellar pearlitic steel has a long flow path before the occurrence of some mechanical deterioration. This agrees with the solid mechanical efficiency under successive bending deformations of the studied lamellar pearlitic steel (SR400).

Conversely, the replacement of shear bands per small recrystallized grains during the stress relief treatment at 700 $^{\circ}\text{C}$ in the SR700 condition may also cause strain concentration. However, it may bring an earlier mechanical degradation. In view of this, a recent study [8] has reported the propagation of macro cracks between small recrystallized grains in pearlitic steel manufactured similarly to the SR700 in the present work. In this case, the authors showed that the zones comprised of small recrystallized grains were prone to microcracks nucleation. Also, the authors mentioned that this event was a consequence of the dissimilar capacity of plastic deformation between the small new grains and the local susceptibility of strain-hardening and pill-ups of dislocation because of the large local density of high-angle boundaries in the zone of small recrystallized grains. In addition to this, the Li et al. [67] have concluded that coarse spheroidized cementite particles at the ferritic grains can negatively affect the ductility of pearlitic steel. Moreover, Maeda et al. [68] investigated the formation of voids under tensile test in spheroidized carbon steel with cementite particles located at the ferritic grain boundaries and triple junctions. In this case, the researchers observed two types of voids: one nucleated at the interfaces between ferrite and cementite particles, while the other was cracking the cementite particle itself. Therefore, it is plausive to assume that the presence of spheroidized and coarse cementite particles (hard particles) at the ferritic grain boundaries and triple junctions around softer grains with divergences of deformation and strain concentration may cause damage (voids) initiation and finally, the earlier failure of the component under repeated bending condition. This supports the sooner failure of the SR700 specimen.

3.4. Fractured surfaces after the in-situ three-point bending (TPB) experiments

The purpose of the present topic is to explore the fracture surfaces of SR400 (Fig. 14) and SR700 (Fig. 15) specimens after their failure

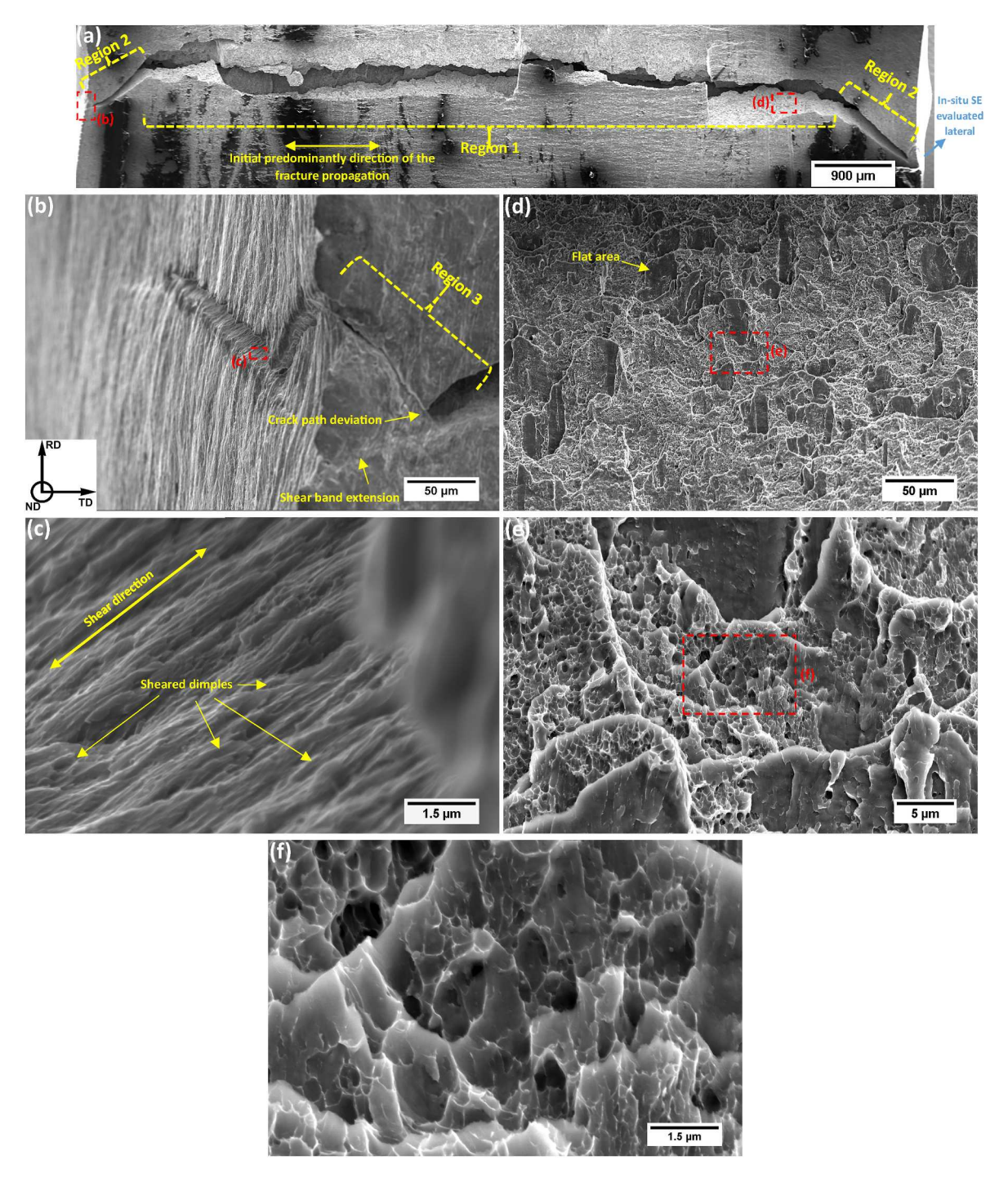


Fig. 14. Scanning electron microscope (SEM) fractographic observation of the SR400 specimen after the cyclic in-situ three-point bending test. (a) Overview of the SR400 bending fracture on the RD-TD surface. (b) Fracture region in the edge of the SR400 specimen. (c) Fracture surface of the crack in the lateral section (RD-ND). (d) (e) (f) Fracture surface, in different magnifications, of the crack in the RD-TD area.

obtained from the fourth cyclic TPB (B4) experiment. In this way, Figs. 14(a) and Fig. 15(a) exhibited the macro view of the cracks in the outer top surfaces (RD-TD) of SR400 and SR700, respectively. In this regard, the fractures presented an almost U-like shape on the RD-TD surface, with their concavities pointed in opposite directions due to their nucleation on the inverse side of the loading pin. Therefore, the concavities of both fracture conditions were positioned down in Figs. 14 (a) and Fig. 15(a) to allow a more accessible visual comparison. These U-like cracks were likely caused by the combined effect of the tensile stress parallel to the RD direction (Region 1) and the formation of shear bands near the edge zones (Region 2).

Regarding Region 1 and Region 2 in Figs. 14(a) and Fig. 15(a), the tensile stress, parallel to the RD direction, may have highly stretched the RD-TD surface, resulting in an abrupt tearing and nucleation of a large crack that follows an almost linear pattern (Region 1). At this failure instant, the quickly nucleated fracture already has a considerable depth in the TD direction. Then, the defects grow secondarily into the lateral surfaces (RD-ND), accompanying the trend of shear bands (Region 2) that are regularly formed around the edge zones during bending experiments [27,28,59,60]. This secondary growth achieved the RD-ND lateral areas 251.7 and 268.1 μm below the top outer surface, respectively, for SR400 and SR700, as previously shown in Fig. 8(b) and (b).

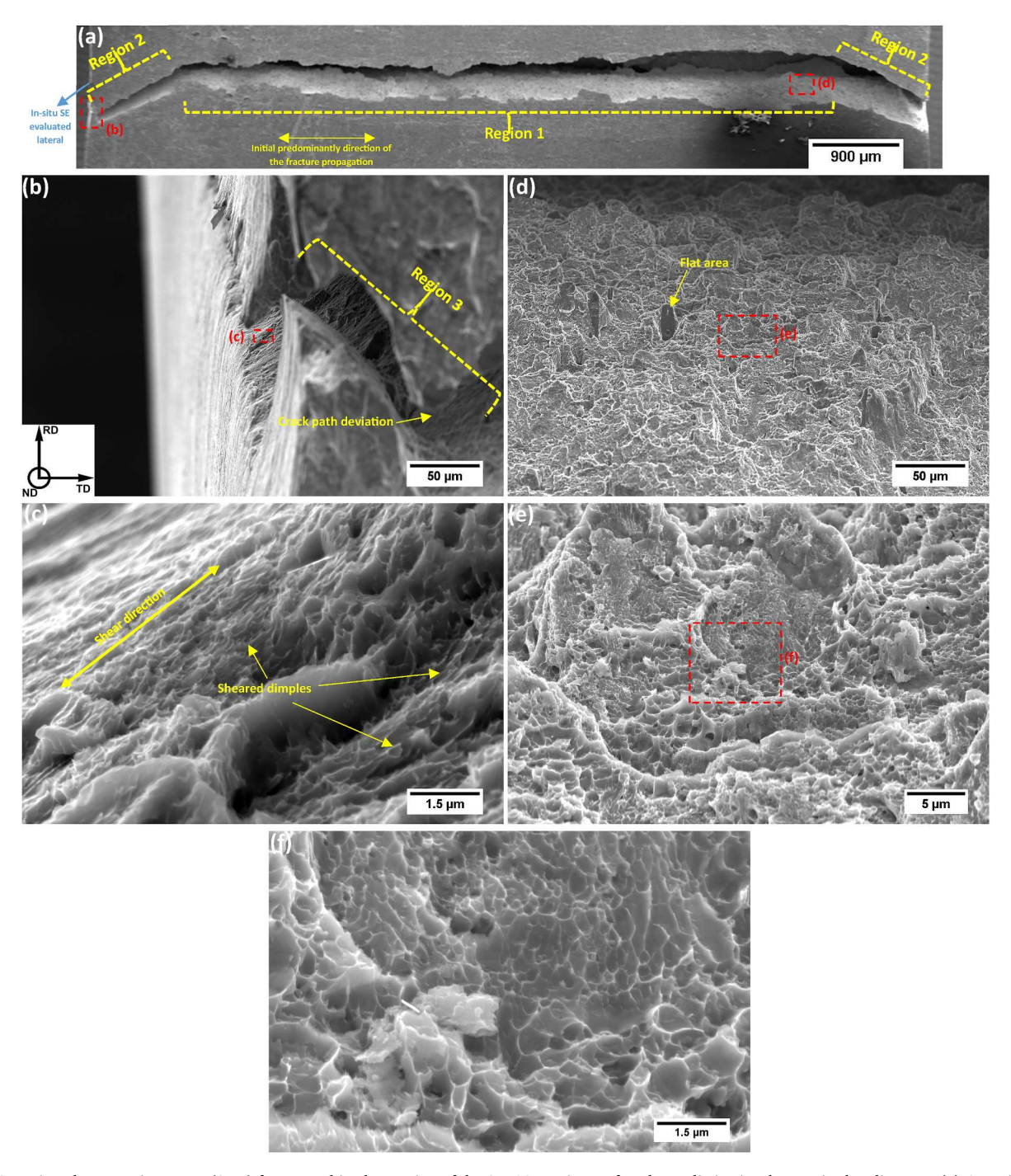


Fig. 15. Scanning electron microscope (SEM) fractographic observation of the SR700 specimen after the cyclic in-situ three-point bending test. (a) Overview of the SR700 bending fracture on the RD-TD surface. (b) Fracture region in the edge of the SR700 specimen. (c) Fracture surface of the crack in the lateral section (RD-ND). (d) (e) (f) Fracture surface, in different magnifications, of the crack in the RD-TD area.

This event may relieve the structural stress in the remaining uncracked border zone. Therefore, it is possible to observe in Figs. 14(b) and Fig. 15 (b) that the cracks changed their pathway in the edge region (Region 3), forming a final zig-zag profile. In this case, the structural stress relief and the potential presence of X-shear bands [69,70] in the border area may have induced the crack deviation by tracking a lower energy path-way.

Furthermore, it can be seen that the fracture propagation into the lateral surfaces (ND-RD) was smoother for SR700 in comparison to the SR400 condition. This demonstrates an easier crack path for the SR700 that collaborates with its earlier collapse in relation to the SR400 condition. In view of this, the two evaluated fracture surfaces (Figs. 14 and 15) occurred under distinct bending circumstances due to the divergent

mechanical properties of the two studied pearlitic steel specimens. For this reason, the SR400's failure happened on the outer top surface under greater curvature and higher loading stress compared to the breakdown scenario provided by SR700 (see Figs. 8 and 9). These particular bending divergences, at the failure instant, can affect the shear influence on the structural collapse and, consequently, the morphological aspect of the fractured surfaces.

Therefore, Fig. 14(c) (for SR400) and Fig. 15(c) (for SR700) exhibit the surfaces of the cracks in the DR-ND macro view, previously shown in Figs. 14(b) and Fig. 15(b). In this case, the cracks have internal tilted surfaces that follow the orientation of the Region 2 cracks. This implies that from the spot where the breaks achieved the DR-ND areas, the

cracks propagated toward the bottom side following the angular profile fracture of Region 2 in the zones close to the DR-ND laterals. Moreover, the dimples in Fig. 14(c) are highly stretched and elongated in a direction almost parallel to the SR400 fracture surface. This indicates an intense plastic deformation caused by the shear process. In this case, the microstructural shearing reduces the stress concentration around the voids initially nucleated under the maximum normal tensile stress. Consequently, this mechanism activates the shear bands among the voids' links that are propagated in the direction of the maximum shear stress. In this way, the voids will be shear-linked up, and a final fractured surface with voids in a parabolic and elongated shape will be obtained [71]. Likewise, the dimples on the SR700 surface of Fig. 15(c) were found also sheared, however, to a lesser degree. Based on this, the almost straight failure position of SR700 may minimize the effect of any shear component. Also, this outcome confirms that the Region 2 fracture, near the laterals, is developed with some influence of the shear process.

Furthermore, the surface of Region 1 fracture in the SR400 failure (Fig. 14(d), (e), and Fig. 14(f)) depicted the presence of many dimples together with a considerable amount of local flat zones poor in dimples. In this regard, Li et al. [72] reported that when local shear plastic deformation is enormous, the maximum normal tensile component cannot produce the initial voids. Instead, the void nucleation is replaced by an accumulated plastic slippage that occurs by activating many shear bands. In this context, the concentrated propagation of the local high-strained bands will promote the forming of an integrated shear fracture surface deficient in dimples [73]. On the other hand, Region 1 of the SR700 fissure provided substantially fewer flat areas (see Fig. 15 (d), (e), and Fig. 15(f)) than the same region of the SR400 fracture. This contrasting shear influence on the fractured surfaces of SR400 and SR700 may result from the divergent geometric failure position of both specimens. In more detail, Figs. 14(f) and Fig. 15(f) display dimples from Region 1, respectively, in a stretched ellipsoidal morphology into RD direction for SR400 and no elongated round shape for SR700. This indicates that the SR400 dimples underwent a more significant plastic deformation in relation to the SR700 ones. In general, the micrographs demonstrate that both studied conditions had a ductile failure mode. However, it is plausible to acknowledge that the SR400 holds a higher severe level of plastic deformation before its collapse, while the SR700 does not.

4. Conclusion

In this study, secondary electron imaging and electron backscattered diffraction (EBSD) techniques were performed, respectively, during insitu and interrupted cyclic three-point bending (TPB) tests in pearlitic steel. Two conditions of pearlitic steel were designed for the TPB experiments: stress-relieved at 400 (SR400) and 700 $^{\circ}\text{C}$ (SR700) for 60 s after introducing 65 % cold rolled reduction. The conclusions are summarized below.

- The employment of a high-stress relief temperature (700 °C) under a short time (60 s) in a 65 % cold rolled pearlitic steel significantly modified its microstructure. Instead, a low-stress relief temperature (400 °C) for the same period of time (60 s) did not provide any meaningful metallurgical modification.
 - •The lamellar pearlitic steel condition (SR400) exhibited mechanical and microstructural stability under repeated TPBs. In contrast, the partially spheroidized pearlitic steel condition (SR700) was prone to softening during cyclic TPB deformation.
 - •The replacement of the lamellar pearlitic design with shear bands by the partially spheroidized pearlitic architecture with recrystallized small grain zones made the pearlitic steel susceptible to earlier development of macro shear band and failure during the fourth successive TPB step.

- •Shear bands and small ferritic recrystallized grain zones were the main strain concentration regions found, respectively, for SR400 and SR700 specimens during the successive TPB experiments.
- •The zones full of fine recrystallized grains with coarse and hard second-phase particles were considered the potential cause of the earlier damage and failure of the SR700 pearlitic steel condition during the successive TPB experiments.
- •SR400 experienced a higher degree of plastic deformation and great influence of the shear component in comparison to SR700 before their failure during the fourth consecutive bending step. As a consequence, the fractured surface of SR400 was comprised of many sheared areas together with elongated dimples while the SR700's fractography was constituted predominantly by no stretched round dimples."

Data availability

Data will be made available on request.

Declaration of competing interest

The authors declare that they have no known competing financial interests or personal relationships that could have appeared to influence the work reported in this paper.

Acknowledgments

The authors kindly acknowledge the following researcher groups, facilities, and fund support institutions: Materials Characterization Laboratory (LACAM), Analytical Central from Federal University of Ceará (UFC), the Ohio State University (OSU), the Manufacturing and Materials Joining Innovation Center (MA²JIC), the Center for Electron Microscopy and Analysis (CEMAS), the Research and Support Foundation of Maranhao (FAPEMA), Brazilian Federal Agency for Support and Evaluation of Graduate Education (CAPES) and Brazilian National Council for Scientific and Technological Development (CNPq).

References

- EP 0 232 558 B1. Europe patent specification: process for manufacturing pearlitic steel wire, 1990.
- [2] EP 0 478 771 B1. Fascicule de brevet europeen: Procede d'elaboration de fils d'acier destines a la fabrication de conduites flexibles, fils d'acier obtenus par ce procede et conduites flexibles renforcees par de tels fils. 1996.
- [3] Fernando US, Davidson M, Yan K, Roy MJ, Pirling T, Withers PJ, et al. Evolution of residual stress in tensile armour wires of flexible pipes during pipe manufacture. In: Proceedings of the ASME 2017 36th international conference on ocean. Trondheim, Norway: Offshore and Arctic Engineering; 2017 Jun 25-30.
- [4] Allain SYP, Roth A, Bauaziz O, D'Eramo E. Microstructure-based behavior law for globular pearlitic steels. J Mater Res Technol 2019;8:3373–6. https://doi.org/ 10.1016/j.jmrt.2019.03.014.
- [5] Figueiredo RB, Langdon TG. Deformation mechanisms in ultrafine-grained metals with an emphasis on the Hall-Petch relationship and strain rate sensitivity. J Mater Res Technol 2021;14:137–59. https://doi.org/10.1016/j.jmrt.2021.06.016.
- [6] Aranda MM, Kim B, Rementeria R, Capdevila C, de Andrés CG. Effect of prior austenite grain size on pearlite transformation in a hypoeuctectoid Fe-C-Mn steel. Metall Mater Trans 2014;45A:1778–86. https://doi.org/10.1007/s11661-013-1996-0
- [7] Allain S, Bouaziz O. Microstructure based modeling for the mechanical behavior of ferrite–pearlite steels suitable to capture isotropic and kinematic hardening. Mater Sci Eng 2008:496:329–36. https://doi.org/10.1016/j.msea.2008.06.009.
- [8] Leão PBP, Zhang S, Neto JRB, Freire SA, Loureiro RdeCP, Ramirez AJ, et al. Microstructure, microtexture, and crack susceptibility in pearlitic steel during labsimulated processes aiming tensile armor application in flexible pipelines. J Mater Process Technol 2023;316:117950. https://doi.org/10.1016/j. imatprotec.2023.117950.
- [9] Stodolny J, Golaszewski A, Łotarewicz A. Fragmentation rate of cementite lamellas in nanopearlite. J Occup Med 2019;71:3298–304. https://doi.org/10.1007/ s11837-019-03655-w.
- [10] Yi HL, Hou ZY, Xu YB, Wu D, Wang GD. Acceleration of spheroidization in eutectoid steels by the addition of aluminum. Scripta Mater 2012;67:645–8. https://doi.org/10.1016/j.scriptamat.2012.07.020.
- [11] Verhoeven JD, Gibson ED. The divorced eutectoid transformation in steel. Metall Mater Trans A 1998;29:1181–9. https://doi.org/10.1007/s11661-998-0245-4.

- [12] Sun J-J, Lain F-L, Liu H-j, Jiang T, Guo S-W, Du L-X, et al. Microstructure of warm rolling and pearlitic transformation of ultrafine-grained GCr15 steel. Mater Char 2014;95:291–8. https://doi.org/10.1016/j.matchar.2014.07.011.
- [13] Prasad C, Bhuyan P, Kaithwas C, Saha R, Mandal S. Microstructure engineering by dispersing nano-spheroid cementite in ultrafine-grained ferrite and its implications on strength-ductility relationship in high carbon steel. Mater Des 2018;139: 324–35. https://doi.org/10.1016/j.matdes.2017.11.019.
- [14] Furuhara T, Mizoguchi T, Maki T. Ultra-fine (α+θ) duplex structure formed by cold rolling and annealing of pearlite. ISIJ Int 2005;45:392–8. https://doi.org/10.2355/ isijinternational.45.392.
- [15] Tomota Y, Watanabe O, Kanie A, Moriai A, Minakawa N, Moriai Y. Effect of carbon concentration on tensile behavior of pearlitic steels. Mater Sci Technol 2003;19: 1715–20. https://doi.org/10.1179/026708303225008310.
- [16] Kanie A, Tomota Y, Torii S, Kamiyama T. Elastic strains of cementite in a pearlite, steel during tensile deformation measured by neutron diffraction. ISIJ Int 2004;44: 1952–6. https://doi.org/10.2355/isijinternational.44.1952.
- [17] Mouritz AP. Introduction to aerospace material. Cambridge: Woodhead Publishing Limited; 2012.
- [18] Rastegari H, Kermanpur A, Najafizadeh A. Effect of initial microstructure on the work hardening behavior of plain eutectoid steel. Mater Sci Eng 2015;632:103–9. https://doi.org/10.1016/j.msea.2015.02.040.
- [19] Yasuda Y, Ohashi T, Shimokawa T, Niiyama T. Strain-hardening characteristics of ferrite layers in pearlite microstructure. Mater Sci Technol 2017;34:772–9. https://doi.org/10.1080/02670836.2017.1397941.
- [20] Li YJ, Choi P, Goto S, Borchers C, Raabe D, Kirchheim R. Evolution of strength and microstructure during annealing of heavily cold-drawn 6.3 GPa hypereutectoid pearlitic steel wire. Acta Mater 2012;60:4005–16. https://doi.org/10.1016/j. actamat.2012.03.006.
- [21] Zheng H, Fu L, Ji X, Ding Y, Wang W, Wen M, et al. Microstructural evolution and mechanical property of ultrafine-grained pearlitic steel by cold rolling: the influence of cementite morphology. Mater Sci Eng 2021;824:141860. https://doi. org/10.1016/j.msea.2021.141860.
- [22] Zhou L, Fang F, Wang L, Hu X, Xie Z, Jiang J. Torsion performance of pearlitic steel wires: effects of morphology and crystallinity of cementite. Mater Sci Eng 2019; 743:425e35. https://doi.org/10.1016/j.msea.2018.11.113.
- [23] Tagashira S, Sakai K, Furuhara T, Maki T. Deformation microstructure and tensile strength of cold rolled pearlitic steel sheets. ISIJ Int 2000;40(11):1149e56. https://doi.org/10.2355/isijinternational.40.1149.
- [24] Krauss G, Matlock DK. Effects of strain hardening and fine structure on strength and toughness of tempered martensite in carbon steels. J Phys IV 1995;5:51–9. https://doi.org/10.1051/jp4:1995806.
- [25] Hanonge D, Ferraz J-P, Ferré R. CO₂-Stress corrosion cracking risk mitigation for flexible pipe design. In: Subsea pipeline technology congress; 2022 Mar 29. London. United Kingdom.
- [26] Kapp MW, Renk O, Eckert J, Pippan R. The importance of lamellar architecture to obtain ductility in heavily cold-worked pearlitic steels revealed by microbending experiments. Acta Mater 2022;232:117935. https://doi.org/10.1016/j. actamat 2022 117935
- [27] Saastamoinen A, Kaijalainen A, Porter D, Suillanen P. The effect of thermomechanical treatment and tempering on the subsurface microstructure and bendability of direct-quenched low-carbon strip steel. Mater Char 2017;134: 172–81. https://doi.org/10.1016/j.matchar.2017.10.020.
- [28] Arola A-M, Kaikalainen A, Kesti V, Troive L, Larkiola J, Porter D. The effect of mechanical behavior on bendability of ultrahigh-strength steel. Mater Today Commun 2021;26:101943. https://doi.org/10.1016/j.mtcomm.2020.101943.
- [29] Wang Y, Tomota Y, Harjo S, Gong W, Ohmura T. In-situ neutron diffraction during tension-compression cyclic deformation of a pearlite steel. Mater Sci Eng 2016;676: 522–30. https://doi.org/10.1016/j.msea.2016.08.122.
- [30] Humphreys J, Rohrer SG, Rollett A. Recrystallization and related annealing phenomena recrystallization and related annealing phenomena. third ed. Amsterdam: Elsevier; 2017.
- [31] Aksenova K, Gromov V, Ivanov Y, Qin R, Vashchuk E. Structural phase transformation of rail steel in compression. Metals 2022;12:1–11. https://doi.org/ 10.3390/met12111985.
- [32] Tung P-Y, Zhou X, Mayweg D, Morsdorf L, Herbig M. Under-stoichiometric cementite in decomposing binary Fe-C pearlite exposed to rolling contact fatigue. Acta Mater 2021;216:117144. https://doi.org/10.1016/j.actamat.2021.117144.
- [33] Montana Y, Idoyaga Z, Gutiérrez I, Iza-Mendia A. Pearlite spheroidisation and microstructure refinement through heavy warm deformation of hot rolled 55VNb microalloyed steel. Metall Mater Trans A 2022;53:2586–99. https://doi.org/ 10.1007/s11661-022-06688-0.
- [34] Lupton DF, Warrington DH. The influence of deformation on the spheroidization and coarsening of pearlite. Sci J 1972;6:200–4. https://doi.org/10.1179/ 030634572790445849.
- [35] Cottrell AH, Bilby B. Dislocation theory of yielding and strain ageing of iron. Proc. Phys Soc London Sect A 1949;62:49–62. https://doi.org/10.1088/0370-1298/62/ 1/308
- [36] Takahashi J, Kosaka M, Kawakami K, Tarui T. Change in carbon state by low-temperature aging in heavily drawn pearlitic steel wires. Acta Mater 2012;60: 387–95. https://doi.org/10.1016/j.actamat.2011.09.014.
- [37] Johnson RA. Clustering of carbon atoms in α -iron. Acta Metall 1967;15:513–7. https://doi.org/10.1016/0001-6160(67)90084-3.
- [38] Ventelon L, Lüthi B, Clouet E, Proville L, Legrand B, Rodney D, et al. Dislocation core reconstruction induced by carbon segregation in bcc iron. Phys Rev B 2015; 91:220102. https://doi.org/10.1103/PhysRevB.91.220102.

- [39] Wright S, Nowell M, Field D. A review of strain analysis using electron backscatter diffraction. Microsc Microanal 2011;17:316–29. https://doi.org/10.1017/ S1431927611000055.
- [40] Mishra K, Khiratkar VN, Singh A. Change of deformation mechanism through nanostructuring of pearlite: an in-situ study. Mater Char 2020;167:110487. https://doi. org/10.1016/j.matchar.2020.110487.
- [41] Li YJ, Choi P, Borchers C, Westerkamp S, Goto S, Raabe D, et al. Atomic-scale mechanisms of deformation-induced cementite decomposition in pearlite. Acta Mater 2011;59(10):3965e77. https://doi.org/10.1016/j.actamat.2011.03.022.
- [42] Hosford WF. Mechanical behavior of materials. Cambridge: Cambridge University press; 2005.
- [43] Becton M, Wang X. Grain-size dependence of mechanical properties in polycrystalline boron-nitride: a computational study. Phys Chem Chem Phys 2015; 17:21894. https://doi.org/10.1039/C5CP03460D.
- [44] Yu H, Wu HY, Chu ZK. Effect of loading-path on the elastic modulus degradation of high strength steels. IOP Conf Ser Mater Sci Eng 2022;1270:012042. https://doi. org/10.1088/1757-899X/1270/1/012042.
- [45] Yu HY. Variation of elastic modulus during plastic deformation and its influence on springback. Mater Des 2009;30:846–50. https://doi.org/10.1016/j. matdes 2008 05 064
- [46] Gensamer M, Pearsall EB, Pellini WS, Low Jr JR. The tensile properties of pearlite, bainite, and spheroidite. Metallogr Microstruct Anal 2012;1:171–89. https://doi. org/10.1007/s13632-012-0027-7.
- [47] Zheng C, Li L, Yang W, Sun Z. Microstructure evolution and mechanical properties of eutectoid steel with ultrafine or fine (ferrite + cementite) structure. Mater Sci Eng 2014;599:16–24. https://doi.org/10.1016/j.msea.2014.01.037.
- [48] Guziewski M, Coleman SP, Weinberger CR. Atomistic investigation into the atomic structure and energetics of the ferrite-cementite interface: the Bagaryatskii orientation. Acta Mater 2016;119:184–92. https://doi.org/10.1016/j. actamat.2016.08.017.
- [49] Zhang M-X, Kelly PM. Accurate orientation relationships between ferrite and cementite in pearlite. Scripta Mater 1997;37:2009. https://doi.org/10.1016/ S1359-6462(97)00396-5. –15.
- [50] Zhou DS, Shiflet GJ. Ferrite: cementite crystallography in pearlite. Metall Trans A 1992;23:1259–69. https://doi.org/10.1007/BF02665057.
- [51] Dippenaar RJ, Honeycombe RWK. The crystallography and nucleation of pearlite. Proc Math Phys Eng Sci P Roy Soc A-Math Phy 1973;333:455–67. https://doi.org/10.1098/rspa.1973.0073.
- [52] Zhou DS, Shiflet GJ. A new orientation relationship between austenite and cementite in an Fe-C-Mn steel. Scripta Metall Mater 1992;27:1215–8. https://doi. org/10.1016/0956-716X(92)90602-B.
- [53] Benito JA, Manero JM, Jorba J, Roca A. Change of Young's modulus of cold deformed pure iron in a tensile test. Metall Mater Trans A 2005;36:3317–24. https://doi.org/10.1007/s11661-005-0006-6.
- [54] Chatti S, Fathallah R. A study of the variations in elastic modulus and its effect on springback prediction. Inter J Mater Form. Int J Mater Form 2012;7:19–29. https://doi.org/10.1007/s12289-012-1106-7.
- [55] Naofal J, Naeini HM, Mazdak S. Effects of hardening model and variation of elastic modulus on springback prediction in roll forming. Metals 2019;9:1005. https://doi.org/10.3390/met9091005.
- [56] Gau J-T, Kinzel GL. An experimental investigation of the influence of the Bauschinger effect on springback predictions. J Mater Process Technol 2001;108: 369–75. https://doi.org/10.1016/S0924-0136(00)00834-7.
 [57] Yang X, Choi C, Sever NK, Altan T. Prediction of springback in air-bending of
- [57] Yang X, Choi C, Sever NK, Altan T. Prediction of springback in air-bending of Advanced High Strength steel (DP780) considering Young's modulus variation and with a piecewise hardening function. Int J Mech Sci 2016;105:266–72. https://doi. org/10.1016/j.ijmecsci.2015.11.028.
- [58] Zhuang Z, Liu Z, Cui Y. Dislocation mechanism-based crystal plasticity: theory and computation at the micron and submicron scale. London: Academic Press; 2019.
- [59] Bjørn HF, Lodgaard L, Langsrud Y, Børvik T, Hopperstad OS. Influence of local microstructural variations on the bendability of aluminum extrusions: experiments and crystal plasticity analyses. J Appl Mech 2022;90:04006. https://doi.org/ 10.1115/1.4056429.
- [60] Muhammad W, Kang J, Brahme AP, Ali U, Hirsch J, Brinkman H-J, et al. Bendability enhancement of an age-hardenable aluminum alloy: Part I relationship between microstructure, plastic deformation, and fracture. Mater Sci Eng 2019;753:179–91. https://doi.org/10.1016/j.msea.2019.03.053.
 [61] Yajima Y, Koga N, Watanabe C. Influential factors on the deformability of colonies
- [61] Yajima Y, Koga N, Watanabe C. Influential factors on the deformability of colonies in pearlitic steel. Mater Char 2021;177:111197. https://doi.org/10.1016/j. matchar 2021 111197
- [62] Leão PBP, Neto JRB, Rodrigues SF, Novotny L, Cardoso JL, Herculano LFG, et al. In-situ tensile-shear test in SEM and DIC analysis of two pearlitic steel microstructures: undeformed-coarse and deformed-refined. J Mater Res Technol 2023;24:9441–61. https://doi.org/10.1016/j.jmrt.2023.05.154.
- [63] Wright SI, Nowell MM, Field DP. A review of strain analysis using electron backscatter diffraction. Microsc micro 2011;17:316–29. https://doi.org/10.1017/ \$143197611000055
- [64] Wang CJ, Yao BN, Liu ZR, Kong XF, Legut D, Zhang RF, et al. Effects of solutes on dislocation nucleation and interface sliding of bimetal semi-coherent interface. Int J Plast 2020;131:102725. https://doi.org/10.1016/j.ijplas.2020.102725.
- [65] Zhao T-Z, Zhang S-H, Zhang G-L, Song H-W, Cheng M. Hardening and softening mechanisms of pearlitic steel wire under torsion. Mater Des 2014;59:397–405. https://doi.org/10.1016/j.matdes.2014.03.029.
- [66] Technical note EBSD hexagonal data sampling. EDAX smart Insight; 2013 [homepage on the internet] [cited 2023 Oct 6]. Available from: https://www.edax.

- com/-/media/ametekedax/files/ebsd/technical_notes/hexagonal-data-sampling.
- [67] Li Y, Kostka A, Choi P, Goto S, Ponge D, Kirchheim R, et al. Mechanisms of subgrain coarsening and its effect on the mechanical properties of carbon-supersaturated nanocrystalline hypereutectoid steel. Acta Mater 2015;84:110–23. https://doi.org/ 10.1016/j.actamat.2014.10.027.
- [68] Maeda M, Shimamura J, Suzuki S. Effect of cementite dispersion on void formation process in spheroidize-annealed steels. ISIJ Int 2018;58:1490–9. https://doi.org/ 10.2355/isijinternational.ISIJINT-2018-077.
- [69] Niu F, He J, Liu D, Zuo X, Cai M. Effect of bending process on microstructure, mechanical properties and crack formation of 5% Ni steel. Metals 2022;12:1188. https://doi.org/10.3390/met12071188.
- [70] Muhammad W, Brahme AP, Ali U, Hirsch J, Engler O, Aretz H, et al. Bendability enhancement of an age-hardenable aluminum alloy: Part II — multiscale numerical modeling of shear banding and fracture. Mater Sci Eng 2019;754:161–77. https:// doi.org/10.1016/j.msea.2019.03.050.
- [71] Dieter GE. Mechanical metallurgy. third ed. United States: McGraw-Hill book company; 1986.
- [72] Li Z, Shi J, Tang A. Investigation on fracture mechanisms of metals under various stress states. Acta Mech 2014;225:1867–81. https://doi.org/10.1007/s00707-013-1024-x.
- [73] Guo ZG, Ma TJ, Yang XW, Tao J, Li J, Li WY, Vairis A. In-situ investigation on dislocation slip concentrated fracture mechanism of linear friction welded dissimilar Ti17(α + β)/Ti17(β) titanium alloy joint. Mater Sci Eng 2023;872: 144991. https://doi.org/10.1016/j.msea.2023.144991.